A&A, 708, A152 (2026)
https://doi.org/10.1051/0004-6361/202557897
© The Authors 2026

Astronomy & Astrophysics

Extreme equivalent-width-selected low-mass starbursts at z = 4–9: Insights into their role in cosmic reionization

M. Llerena[1,⋆], L. Pentericci[1], R. Amorín[2], A. Ferrara[3], M. Dickinson[4], F. Arevalo-Gonzalez[1,5], A. Calabrò[1], L. Napolitano[1,5], S. Mascia[6], P. Arrabal Haro[7], R. Begley[8], N. J. Cleri[9,10,11], K. Davis[12,13⋆⋆], W. Hu[14,15], J. S. Kartaltepe[16], A. M. Koekemoer[17], R. A. Lucas[17], E. McGrath[18], D. J. McLeod[19], C. Papovich[14,15], T. M. Stanton[19], A. J. Taylor[20,21], R. Tripodi[1], X. Wang[22,23,24], and L. Y. A. Yung[17]

(Affiliations can be found after the references)

Received 29 October 2025 / Accepted 4 March 2026

ABSTRACT

We investigate the properties of extreme emission line galaxies (EELGs) at $z = 4{-}9$ and their role in reionization. Compact, low-mass galaxies with intense optical emission lines are linked to elevated specific star formation rates (sSFRs) and recent bursts of star formation. Feedback in these systems may enable the leakage of ionizing radiation into the intergalactic medium. Using JWST/NIRSpec spectroscopy from the CAPERS, CEERS, and RUBIES surveys, we compiled 160 NIRCam-selected EELGs in the EGS field. These galaxies show extreme rest-frame equivalent widths (EWs), with a median EW([O III]+Hβ) = 1616 Å and EW(Hα) = 763 Å. They are low-mass (median $\log(M_\star/M_\odot) = 8.26$) with high sSFRs (median 43 Gyr^{-1}), above the $z \sim 6$ main sequence. UV slopes are diverse, with a median value of $\beta = -2.0$, and only 7% have extremely blue continua ($\beta < -2.6$). Emission-line diagnostics suggest stellar populations as the primary ionizing source, although an AGN fraction of 14% cannot be entirely ruled out. These galaxies are efficient ionizing photon producers, with median $\log(\xi_{\rm ion}$ [Hz erg^{-1}]) = 25.37, exceeding typical values at similar redshifts. Escape fractions, however, are heterogeneous: 16% of EELGs at $z < 7$ show escape fractions >5% for both Lyα and LyC photons, while 82% lack detectable Lyα emission. The median inferred LyC escape fraction is modest (5%) but enhanced in compact super-Eddington systems with sSFR > 25 Gyr^{-1}. These results indicate that EELGs contribute approximately 16–40% of the total ionizing emissivity required to sustain hydrogen reionization. EELGs are extremely compact, with a median effective radius of 0.49 kpc, and exhibit a recent star formation burst. Our analysis indicates that sSFR and star formation rate surface density are the primary drivers of their extreme emission line strengths.

Key words. galaxies: evolution – galaxies: formation – galaxies: high-redshift – galaxies: ISM – galaxies: starburst

1. Introduction

Extreme emission line galaxies (EELGs) are characterized by intense emission lines that stand out prominently against their stellar continuum, resulting in large rest-frame equivalent widths (EWs). Some examples of these lines include rest-frame optical [O III]λ5007 Å (hereafter [O III]) and Hα. The strong nebular emission lines are typically powered by ionizing photons emitted from massive, short-lived O and B stars or active galactic nuclei (AGNs), while the surrounding rest-frame optical continuum arises mainly from longer-lived, lower-mass stars (e.g. Eldridge & Stanway 2022). Therefore, EW provides insight into the ratio of very young to older stellar populations, serving as an indicator of variations in the star formation history (SFH) over time. Identifying EELGs within a galaxy population can reveal galaxies experiencing a burst in star formation (e.g. Endsley et al. 2024), often characterized by high specific star formation rates (sSFRs) and compact morphologies (e.g. Tang et al. 2022).

Based on the recent Attenuation-Free Model (AFM; Ferrara 2024), elevated sSFR > 25 Gyr^{-1} might be linked to galaxies that become super-Eddington (SE) and trigger a radiation-driven outflow that clears the dust, making the galaxy UV brighter and bluer. The presence of such outflows is crucial for understanding the escape of ionizing Lyman continuum (LyC, $\lambda_{\rm rest} < 912$ Å) photons, as they can create ionized, dust-free channels that enable the leakage of LyC photons (e.g. Hogarth et al. 2020; Amorín et al. 2024; Carr et al. 2025; Komarova et al. 2025). Outflows can significantly increase the visibility of the Lyα line even at $z > 5.5{-}6$ when the intergalactic medium (IGM) is not fully ionized (e.g. Fan et al. 2006; Mason & Gronke 2020). In samples of $z > 7$ galaxies, where in principle Lyα should be strongly attenuated by the neutral IGM, high EW(Lyα) are associated with high sSFRs and ionized bubbles large enough to produce frequency shifting that reduces the effects of resonant scattering for Lyα (e.g. Endsley et al. 2022; Bunker et al. 2023; Tang et al. 2023; Witstok et al. 2025). Evidence of outflows has been observed in samples of [O III] emitters in a wide range of redshifts (e.g. Llerena et al. 2023; Saldana-Lopez et al. 2025; Cooper et al. 2025; Zamora et al. 2025; León Contreras et al. 2026) with a fraction of ~20% of galaxies at $z < 6$ showing signatures of outflows (e.g. Calabrò et al. 2024b; Carniani et al. 2024). Furthermore, strong [O III]$\lambda\lambda$4959, 5007 Å+Hβ (hereafter [O III]+Hβ) emission and high O32=log([O III]/[O II]$\lambda\lambda$3727,3729 Å) have been suggested as a necessary requirement for high escape fractions of LyC photons ($f{\rm esc}_{\rm LyC}$) given that these conditions are observed in a high proportion of confirmed LyC leaking galaxies (e.g. Vanzella et al. 2016; Izotov et al. 2021). Additionally, galaxies that exhibit high EW([O III]) tend to show enhanced ionizing photon production efficiencies ($\xi_{\rm ion}$) at different redshifts (e.g. Chevallard et al. 2018; Tang et al. 2019; Llerena et al. 2025).

⋆ Corresponding author: `mario.llerenaona@inaf.it`

⋆⋆ NSF Graduate Research Fellow.

However, very high $\mathrm{fesc}_{\mathrm{LyC}}$ or very low metallicities could affect the strength of [O III] emission, so the connection is still not fully understood (e.g. Endsley et al. 2023; Laseter et al. 2025).

Due to their extreme emission properties and intense star formation activity, EELGs serve as valuable laboratories for studying the physical conditions and mechanisms that enable the escape of both LyC and Lyα photons, offering key insights into their role in the Epoch of Reionization (EoR). EELGs are observed at different redshifts, from the local universe (e.g. Cardamone et al. 2009; Amorín et al. 2010; Izotov et al. 2011), intermediate redshifts $z \sim 1-3$ (e.g. van der Wel et al. 2011; Amorín et al. 2015; Maseda et al. 2018; Tang et al. 2019; Du et al. 2020; Llerena et al. 2023), and during the EoR (e.g. Smit et al. 2015; De Barros et al. 2019; Boyett et al. 2024; Llerena et al. 2024; Davis et al. 2024; Begley et al. 2025; Daikuhara et al. 2025). These high-EW systems can be identified through either direct spectroscopy or indirect photometric flux excesses, where strong line emission significantly enhances the flux in determined filters. JWST (Gardner et al. 2006, 2023) has enabled highly sensitive near-infrared spectroscopy with NIRSpec (Jakobsen et al. 2022), covering wavelengths up to 5.3 μm. This makes it possible to directly measure rest-frame optical emission lines at high-z, such as Hα up to $z \lesssim 7$ and [O III] up to $z \lesssim 9.5$. These capabilities allow for a robust identification of EELGs and a detailed characterization of their physical properties as spectroscopic samples continue to grow.

In Llerena et al. (2024), a sample of EELG candidates at $z = 4-9$ in the Extended Groth Strip (EGS, 14h19m00s +52°48′00″, Davis et al. 2007) field was identified based on their JWST/NIRCam (Rieke et al. 2023) photometry, specifically using the F277W, F356W, F444W, and F410M filters. The selection was restricted to galaxies with rest-frame EW([O III]+Hβ) > 680 Å motivated by the average spectra of rare, metal-poor starbursts in the local universe (Sánchez Almeida et al. 2012; Pérez-Montero et al. 2021). Based on their photometry, these candidates exhibit low stellar masses, high sSFRs, and compact morphologies, which are characteristics associated with young, rapidly evolving galaxies. In this paper, we analyse the JWST/NIRSpec spectra of a subsample of these candidates to confirm the presence of such extreme emission lines. With this spectroscopic confirmation, we investigate their physical properties, including their ionization conditions and star formation activity, and explore the mechanisms driving the elevated EWs. We further investigate the potential link between strong optical line emission and the production and escape of LyC photons, thereby assessing the role of EELGs in cosmic reionization. Since our analysis is restricted to the EGS field, we note that cosmic variance must be taken into account, as this region has been suggested to be already nearly fully ionized by $z \sim 7$ (e.g. Napolitano et al. 2024; Chen et al. 2025; Napolitano et al. 2026)

This paper is organized as follows. In Sect. 2 we describe the spectroscopic sample selection. In Sect. 3 we outline the procedures for measuring emission lines and the validation of the photometric selection. In Sect. 4 we present the physical properties of the sample based on spectral energy distribution (SED) fitting. We also derive star formation rates from Balmer lines, the rest-frame UV continuum slopes (β), absolute UV magnitudes, the dust reddening, and the gas-phase metallicity. In Sect. 5 we analyse the source of ionization of the EELGs based on emission line diagnostics. In Sect. 6.1 we present the results of the estimated ξ_{ion} in this sample. In Sects. 6.2 and 6.3 we present the results regarding the escape of LyC and Lyα photons, respectively. In Sect. 7 we discuss the potential drivers of the elevated EWs, which include high sSFRs, compactness, and burstiness. Finally, we present our summary and conclusions in Sect. 8.

Throughout this paper, we adopt a Λ-dominated flat universe with $\Omega_\Lambda = 0.7$, $\Omega_{\mathrm{M}} = 0.3$, and $H_0 = 70\,\mathrm{km\,s^{-1}\,Mpc^{-1}}$. All magnitudes are quoted in the AB system (Oke & Gunn 1983). EWs are quoted in the rest-frame and are positive for emission lines. We adopt $\log(\mathrm{O/H})_\odot = 8.69$ (Asplund et al. 2009). We assumed the Kroupa (2001) initial mass function (IMF) for the SED fitting. We report Spearman's correlation coefficients (ρ) with their p-values (p), to assess the strength and significance of correlations.

2. Data and sample selection

In this study, we aim to evaluate the effectiveness of the selection method proposed in Llerena et al. (2024) for identifying EELGs at $z = 4-9$ based on their photometry and then to study their properties to understand the origin of the extreme emission lines. To this end, we construct a subsample of galaxies from the parent sample with available JWST/NIRSpec observations. This includes spectra from the following JWST surveys: the CANDELS-Area Prism Epoch of Reionization Survey (CAPERS, GO-6368; PI Mark Dickinson), the Cosmic Evolution Early Release Science survey (CEERS; Finkelstein et al. 2023, 2024, 2025), and the Red Unknowns: Bright Infrared Extragalactic Survey (RUBIES; de Graaff et al. 2025).

2.1. Selection of the spectroscopic sample

2.1.1. CAPERS sample

CAPERS is an ongoing JWST Cycle 3 Treasury program of moderately deep NIRSpec multiobject spectroscopy in three fields from CANDELS (Grogin et al. 2011; Koekemoer et al. 2011), which includes the EGS field. CAPERS is obtaining low-resolution NIRSpec/PRISM spectra for thousands of distant galaxies, including objects at $z > 10$ (e.g. Kokorev et al. 2025). We cross-matched the list of EELG candidates in Llerena et al. (2024) with the available NIRSpec/PRISM spectra from the CAPERS survey in the EGS field, and we considered the spectra from the data release of the collaboration for the analysis. The data reduction is described in Taylor et al. (2025b). We identified 62 candidates in the survey, but excluded 7 from the sample because their bright emission lines, based on the photometric redshift, coincided with a detector gap. We discarded an additional galaxy because its reduced spectrum was contaminated by a secondary source in the slit.

2.1.2. CEERS and RUBIES samples

We also cross-matched the list of EELG candidates in Llerena et al. (2024) with the available spectra in the Public NIRSpec datasets (v3) published on the DAWN JWST Archive (DJA[1]; Heintz et al. 2024; de Graaff et al. 2025) and we used the NIRSpec data reduced by the Cosmic Dawn Center. In particular, we selected galaxies from the CEERS and RUBIES surveys with NIRSpec/PRISM and NIRSpec/G395M (medium resolution, MR) spectra. Regarding the CEERS subsample, we found 32 galaxies with PRISM spectra in the DJA database. We excluded 3 galaxies because their bright emission lines

---

[1] `https://dawn-cph.github.io/dja/spectroscopy/nirspec/`

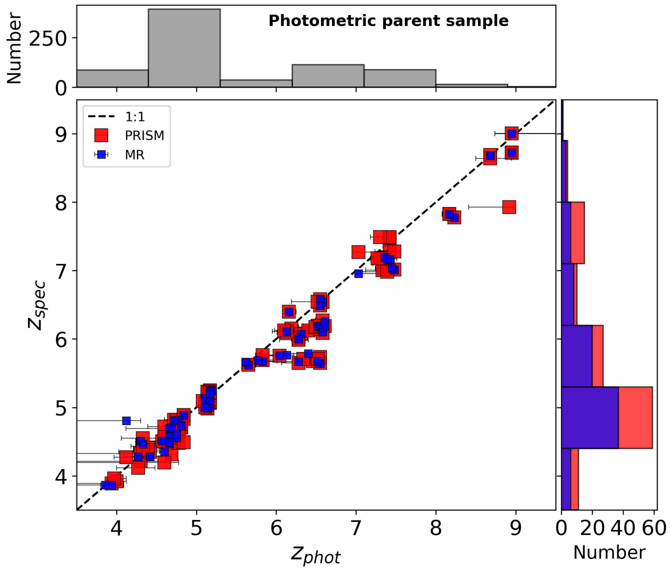

Fig. 1. *Middle*: comparison between $z_{\rm phot}$ and $z_{\rm spec}$ in the sample of selected EELGs. The dashed black line is the 1:1 relation. *Right*: distribution of $z_{\rm spec}$, shown as superimposed histograms. In both panels, in red (blue), the galaxies with PRISM (MR) spectra. *Top*: distribution of $z_{\rm phot}$ in the photometric parent sample (Llerena et al. 2024).

coincide with a detector gap, as determined by the photometric redshift. We also found 10 galaxies with MR spectra. Regarding the RUBIES subsample, we identified 48 galaxies with PRISM spectra in the DJA database, excluding 4 because of the detector gaps, as in the CEERS subsample. In addition, we found 76 galaxies with MR spectra and excluded 5 of them for the same reason.

In summary, our final sample consists of 208 spectra: 127 EELG candidates observed with the PRISM configuration and 81 with the MR configuration. A subsample of 42 galaxies was observed in both PRISM and MR within CEERS and RUBIES, for which we analyse both spectra. Additionally, two galaxies are included in both CAPERS and RUBIES, and four more are observed in both CEERS and RUBIES. Given the small overlap among surveys, we retain all spectra in our analysis. Therefore, the final sample comprises 160 unique galaxies. The coordinates of the galaxies, the corresponding survey and disperser, are listed in Table A.1. Throughout this paper, individual galaxies are identified using their IDs from the CEERS photometric catalogue.

2.2. Spectroscopic redshifts

As a first step, we assessed the accuracy of the photometric redshifts ($z_{\rm phot}$). To this aim, we used LiMe[2] (Fernández et al. 2024), a library that provides a set of tools to fit lines in astronomical spectra, to estimate the spectroscopic redshifts ($z_{\rm spec}$) in both the PRISM and MR spectra. We assumed a single Gaussian for each line and a local linear continuum, with [O III]+Hβ modelled together as three blended Gaussians (see two showcases in Fig. B.1), while Hα was modelled with a Gaussian profile, merged (blended) with [N II]$\lambda\lambda$6548,6583 Å for PRISM (MR) spectra. We adopted $z_{\rm phot}$ as an initial estimate of the redshift. We determined the observed central wavelength of the Gaussian fits of [O III] to calculate $z_{\rm spec}$. When [O III] is not covered by the spectral range, the observed central peak of Hα is used to determine $z_{\rm spec}$. The distribution of $z_{\rm spec}$ of the sample is displayed in the right panel in Fig. 1 and reported in Table A.1. The sample covers redshifts from $z = 3.86$ to $z = 9.00$ with a median $z = 5.22$ ($\sigma = 1.17$). We note that the peak of the $z_{\rm spec}$ distribution approximately coincides with the peak of the $z_{\rm phot}$ distribution of the photometrically selected parent sample (top panel of Fig. 1).

In the central panel in Fig. 1 we show a comparison between $z_{\rm phot}$ and $z_{\rm spec}$, including the 1σ uncertainty of the $z_{\rm phot}$ based on their probability distribution functions (Finkelstein et al. 2023). We find a good agreement ($\rho = 0.97$, $p \sim 0$) between both quantities with a mean $\Delta z = z_{\rm phot} - z_{\rm spec} = 0.13$ ($\sigma = 0.23$), considering only one spectrum per galaxy in cases where a galaxy has both PRISM and MR spectra. The galaxies at $z \sim 4$ with large $z_{\rm phot}$ uncertainties often have low-z solutions with high probability, which are ruled out by the spectroscopic data. We highlight that no catastrophic outliers with $\Delta z > 3$ are found. We note that larger Δz are observed at $z \sim 6{-}7$. In this range, [O III]+Hβ falls within the F356W filter, while Hα lies in the broader F444W filter. Although the F410M filter sits between them, it primarily samples the continuum rather than overlapping a strong spectral feature, and thus provides limited improvement in redshift precision. The combination of these two broad filters appears to result in less accurate $z_{\rm phot}$ estimates compared to the $z \sim 4{-}6$ range, where Hα may be captured by the narrower F410M filter, or where strong emission lines fall into the F277W and F356W filters, both of which are narrower than F444W.

3. Data analysis

Before proceeding with the spectral analysis, and given the different data reduction applied to the sample, we evaluate potential slit losses by comparing NIRCam photometry with synthetic photometry derived from the spectra. This consistency check ensures that the extracted spectra are properly calibrated and that any significant discrepancies, potentially arising from slit losses or extraction artefacts, are identified and corrected. We used the same photometry described in Sect. 4.1. We find that, on average, the correction factor, defined as the ratio between observed and synthetic photometry, does not show a significant wavelength dependence, which is consistent with previous works (e.g. Roberts-Borsani et al. 2024; Napolitano et al. 2025), and yields a median value of 1.21. Therefore, to account for slit losses, we scale each spectrum by a constant correction factor, which is unique to each galaxy and calculated as the uncertainty-weighted median of the correction factors across all observed filters for that galaxy.

3.1. Emission line measurements

To determine $z_{\rm spec}$ in Sect. 2.2, we fit only the bright [O III]+Hβ and Hα emission lines. In order to measure fluxes of additional emission lines, we then performed a second set of measurements with LiMe, fixing $z_{\rm spec}$ to the value derived in Sect. 2.2. In Figs. C.1 and C.2, we display the median spectra of galaxies observed with PRISM and MR, respectively, highlighting key spectral features. We modelled [O II]$\lambda\lambda$3727,3729 (hereafter [O II]) and [Ne III]λ3868 Å (hereafter [Ne III]) in all galaxies using a single Gaussian profile for each line and a local linear continuum, estimated from 100 Å (50 Å)-wide windows on either side of each line for the PRISM (MR) data. For lines with a signal-to-noise ratio (S/N) below 3, we adopt a 3σ upper limit.

---

[2] `https://lime-stable.readthedocs.io/en/latest/`

To estimate the rest-frame EWs of bright emission lines, we use the continuum measured directly from the spectra when it is detected with S/N > 2 (48% of the sample for [O III]+Hβ and 32% of the sample for Hα with PRISM), and propagate both the line flux and continuum uncertainties to derive the uncertainty of EWs. When the continuum is undetected, we adopt the continuum estimated from the SED model (see Sect. 4.1), and derive its uncertainty by propagating the uncertainties of the photometry from the two closest filters in wavelength to each line. On average, the ratio between the continuum measured from the spectra and from the SED model is 0.9−1.1. The EWs and uncertainties of Hβ, [O III] and Hα are reported in Table A.1.

Given the complexity of Lyα, we performed a separate set of measurements using the PRISM spectra, which provide suitable wavelength coverage. Owing to the low spectral resolution of the PRISM, Lyα is modelled within a 2-pixel window centered on the observed emission peak. As a first step, we compute the line flux via direct integration over this window. The continuum is estimated by a linear fit to the red side of Lyα, from 1900 Å to 3 pixels redward of the emission peak. We adopt a 3σ upper limit for Lyα emission if the S/N < 3 or if the measured flux is negative. In our sample, we find 21 galaxies with Lyα in emission (above 3σ), i.e. Lyα emitters (LAE). We note that, in contrast to ground-based observations with larger slit widths, and given the resonant nature of Lyα emission where Lyα photons can scatter to spatial scales exceeding the stellar continuum (e.g. Ning et al. 2024), JWST slit losses of 35% have been reported for Lyα samples at z = 6−7 (Napolitano et al. 2026, and references therein). We adopt this average value to correct for possible Lyα slit losses.

3.2. Confirmation of extreme EWs

In this subsection we focus on validating the selection method used to identify EELG candidates based on photometric criteria. Figure 2 shows a comparison between the EWs measured from the spectra and those estimated from the photometry in Llerena et al. (2024). In the top panel, we display the EW([O III]+Hβ), and we show that there is a moderate correlation (ρ = 0.50, p ~ 0) between the estimation and the spectroscopic confirmation with a median underestimation of 0.11 dex (σ = 0.22) in the photometric values. This indicates that most of the candidates selected in the sample are EELGs with high EWs. We note that in 154 spectra (74%) both [O III] and Hβ are detected, with 93% of them showing EW([O III]+Hβ) > 680 Å which corresponds to the selection threshold adopted in Llerena et al. (2024). In 21 spectra (10%), [O III] is detected while only an upper limit is available for Hβ; among these, 62% present an upper limit in EW([O III]+Hβ) higher than the selection threshold. In 8 spectra (4%), only [O III] is detected while Hβ is not covered by the spectral range, and 75% of these already exhibit lower limits for EW([O III]+Hβ) above the selection threshold. Finally, in 25 spectra (12%), neither [O III] nor Hβ are covered by the analysed spectra.

In summary, excluding the spectra where neither [O III] nor Hβ are covered, the success rate of spectra with EW([O III]+Hβ) above the selection threshold (or consistent upper/lower limits) reaches 89%. For subsequent analysis, we removed galaxies that, based on either measured or limit values, do not fulfill the selection criterion of EW([O III]+Hβ) > 680 Å since these sources were not targeted in photometric selection and would otherwise introduce incompleteness into the sample.

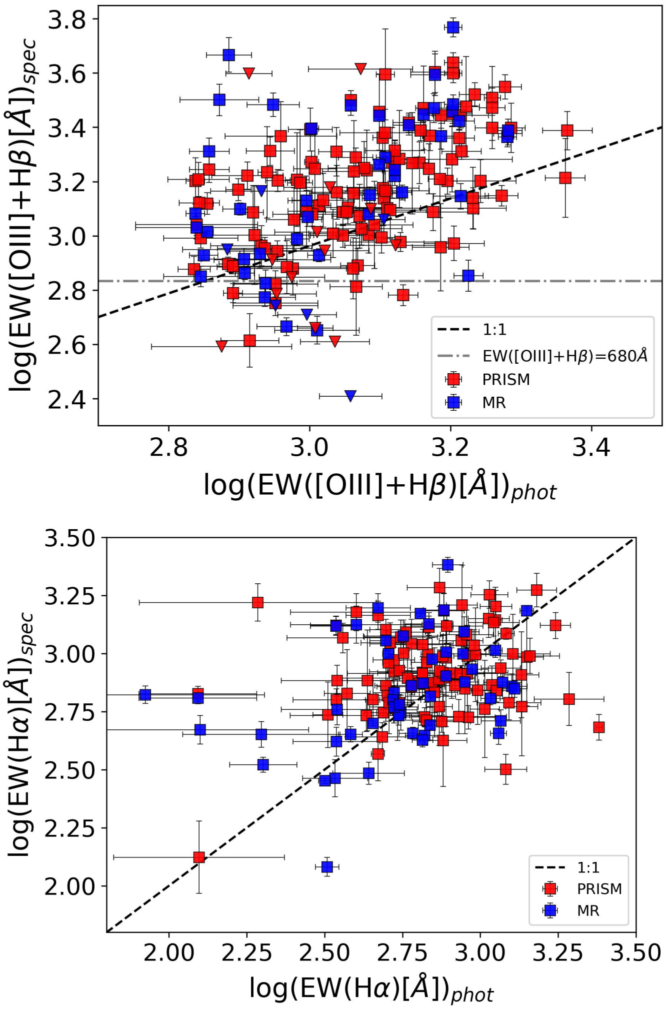

Fig. 2. Comparison between EWs estimated from the photometry and from spectroscopy in the sample of EELGs with PRISM (red squares) or MR (blue squares) spectra. *Top*: EW([O III]+Hβ). The triangle symbols are upper limits due to low S/N of Hβ. The dotted-dashed grey line is the lower limit for the photometric selection. *Bottom:* EW(Hα). The dashed black line is the 1:1 relation.

In this analysed sample, we found a median $\log(\mathrm{EW}([\mathrm{O\,III}]+\mathrm{H}\beta)[\text{Å}]) = 3.20$ (1616 Å) and a 16–84th percentile range from 2.99 to 3.44 (997 to 2785 Å). Such high EWs have been observed in galaxies in the EoR in photometric-selected samples (e.g. De Barros et al. 2019; Daikuhara et al. 2025) and with slitless spectroscopy (e.g. Matthee et al. 2023). Regarding only EW([O III]), we found a median $\log(\mathrm{EW}([\mathrm{O\,III}])[\text{Å}]) = 3.04$ (1095 Å) and a 16–84th percentile range from 2.80 to 3.28 (635 to 1946 Å). In Fig. D.1, we show that EW([O III]) and EW(Hβ) are strongly correlated, suggesting a common source of ionization.

On the other hand, in the bottom panel of Fig. 2, we instead display the comparison with EW(Hα), and we find a weaker correlation (ρ = 0.21, p ~ 8×10^{-3}), but confirm the high EWs estimated from the photometry with a median underestimation of 0.08 dex (σ = 0.44). We found a median $\log(\mathrm{EW}(\mathrm{H}\alpha)[\text{ Å}]) = 2.88$ (763 Å) and a 16–84th percentile range from 2.71 to 3.11 (518 to 1307 Å). The ranges of EWs in the analysed sample are summarized in Table 1. In Fig. D.2, we compared the fluxes and EWs of bright emission lines obtained with each disperser in the subsample with both PRISM and

Table 1. Median properties of the analysed sample of EELGs.

	Median	16–84th interval
EW([O III]+Hβ)[Å]	1616	(997, 2785)
EW([O III])[Å]	1095	(635, 1946)
EW(Hα)[Å]	763	(518, 1307)
$\log(M_\star/M_\odot)$	8.26	(7.84, 8.67)
$\log(\mathrm{SFR}_{\mathrm{Balmer}}[M_\odot\,\mathrm{yr}^{-1}])$	0.90	(0.47, 1.42)
β	−2.00	(−2.33, −1.66)
M_{UV}	−19.17	(−20.12, −18.46)
Stellar $E(B-V)$	0.09	(0.04, 0.15)
$E(B-V)_{\mathrm{neb}}$	0.18	(0.06, 0.30)
log(O/H)+12	7.74	(7.45, 7.90)

Notes. For each parameter, we report the median value and the corresponding 16th and 84th percentiles.

MR spectra. We show that they correlate strongly, with higher PRISM fluxes by ~0.06 dex on average.

4. Characterisation of the sample of EELGs

In this section we investigate the physical properties of the EELGs in our sample. Our analysis incorporates quantities derived from SED fitting, as well as measurements from the spectra, including star formation rates, UV continuum slopes, dust attenuation, and gas-phase metallicities. A summary of the median properties of the analysed sample of EELGs is reported in Table 1.

4.1. Spectral energy distribution fitting

To estimate the physical properties of the galaxies in our sample, namely stellar mass, star-formation rate (SFR), and dust attenuation $E(B-V)$, we update the SED fitting performed in Llerena et al. (2024). First, we used BAGPIPES version 1.2.0 (Carnall et al. 2018) with the Bruzual & Charlot (2003) stellar population models and photometry from the CEERS Photometric Catalogues v0.51.2 (Finkelstein et al. 2025). The photometry was performed with SExtractor (v2.25.0; Bertin & Arnouts 1996) with F277W and F356W as the detection bands. The fiducial fluxes were measured in small Kron apertures corrected by large-scale flux, following the methodology in Finkelstein et al. (2023). The catalogue includes photometric measurements in seven NIRCam filters: F115W, F150W, F200W, F277W, F356W, F410M, and F444W. In addition, it incorporates archival HST imaging of the EGS field from programs such as CANDELS (Koekemoer et al. 2011; Grogin et al. 2011), covering the filters F606W, F814W, F105W, F125W, F140W, and F160W.

We fixed the redshift to z_{spec}. We adopted a non-parametric SFH from Leja et al. (2019), using eight time bins where SFR is fit with a constant value in each bin. The first four bins are set to lookback times of 0–3, 3–10, 10–30, and 30–100 Myr, while the last four bins are logarithmically spaced between 100 Myr and $t_{\max} = t_{\mathrm{universe}}(z = z_{\mathrm{spec}}) - t_{\mathrm{universe}}(z = 20)$. We allow the metallicity to freely vary up to 0.5 $Z_\odot$. The upper limit in metallicity is based on the stellar mass-metallicity relation observed at $z = 3.5$ for a stellar mass of $10^{11}\,M_\odot$ (Llerena et al. 2022; Stanton et al. 2024), which is in agreement with the range of stellar masses of the sample (Llerena et al. 2024). For the dust component, we consider the Calzetti et al. (2000) attenuation curve and let A_V vary between 0–2 mag. We also include a nebular component in the model, and we let the ionization parameter log U freely vary between −4 and 0.

Given that incorporating JWST/MIRI (Wright et al. 2015) detections into SED modelling of galaxies may lower their stellar mass by 0.25 dex at $z = 4$–6 and 0.38 dex at $z = 6$–9 (Papovich et al. 2023), we checked the MIRI imaging provided by CEERS which includes eight pointings, four of which provide deep imaging with the bluer bands (F560W and F770W) and four of which provide contiguous wavelength coverage in F1000W, F1280W, F1500W, and F1800W, where two of these also include coverage in F770W and F2100W (Yang et al. 2023). Only six galaxies in our sample (at $z \sim 4.5$–8.7) are in the MIRI footprint with F560W and F770W imaging, and they have detections in both bands. Although MIRI bands are not included in the SED fitting, we find good agreement, within the uncertainties, between the synthetic photometry from the SED model and the observed F560W and F770W photometry in this subsample, except for one galaxy (ID: 47521) whose observed photometry is larger by a factor of 2.5 compared to the model. This suggests that the SED modelling reliably reproduces the reddest part of the SED, not covered by NIRCam, across the sample of EELGs.

4.2. Star formation rates from Balmer lines

We corrected the line fluxes for dust reddening, adopting the Calzetti et al. (2000) attenuation law, which is consistent with the SED fitting. We considered the stellar $E(B-V)$ value from the SED fitting. A comparison with the nebular $E(B-V)$ obtained by Balmer lines is presented in Sect. 4.5. In particular, we converted the dust-corrected Hα luminosity $L(\mathrm{H}\alpha)$ to SFR assuming the calibration from Shapley et al. (2023) as $\mathrm{SFR(Balmer)}\,[\mathrm{M}_\odot\,\mathrm{yr}^{-1}] = L(\mathrm{H}\alpha)\,[\mathrm{erg\,s}^{-1}] \times 10^{-41.37}$. Some systematics of these calibrations include the IMF and extinction (e.g. Kennicutt & Evans 2012). This is the most suited calibration according to subsolar metallicities expected for our galaxies at $z > 4$. We rescaled these values by a factor of 0.94 (Madau & Dickinson 2014), accounting for the IMF mismatch in the calibration (Chabrier 2003) and in the SED fitting (Kroupa 2001). When Hα is not covered, we used Hβ luminosity assuming Hα/Hβ = 2.79 under case B approximation for $T_e = 15\,000$ K and $n_e = 100\,\mathrm{cm}^{-3}$ (Pérez-Montero 2017). In Appendix E we checked that the estimated SFRs trace the average SFR in the last 10 Myr. We use these Balmer-based SFRs to estimate the sSFRs which are reported in Table A.1.

The distribution of SFR versus $M_\star$ for the sample is shown in Fig. 3. As a reference, we show the main sequence of star-forming (SF) galaxies from Calabrò et al. (2024b) derived from a spectroscopic sample of galaxies in a wide range of redshifts $z = 4$–10. Our sample is scattered above the main sequence (e.g. Speagle et al. 2014; Iyer et al. 2018; Cole et al. 2025), and the galaxies cover ~2 dex in stellar mass and SFR. The sample is composed of low-mass galaxies from $\log(M_\star/M_\odot) = 7.18$ up to $\log(M_\star/M_\odot) = 9.42$, with a median of $\log(M_\star/M_\odot) = 8.26$. This offset above the main sequence is also observed in samples of low-z EELGs (e.g. Calabrò et al. 2017). For comparison, we also plot galaxies at $z = 0.2$–0.4 with LyC detections from the Low-redshift Lyman Continuum Survey (LzLCS; Flury et al. 2022a) and archival programs (Jaskot et al. 2024a,b). Throughout the paper and in subsequent plots, this reference sample is divided into strong ($\mathrm{fesc}_{\mathrm{LyC}} \geq 5\%$) and weak ($\mathrm{fesc}_{\mathrm{LyC}} < 5\%$) LyC leakers. We adopt the 5% threshold to indicate cosmologically significant LyC leakers in order to remain consistent with recent literature (Flury et al. 2022a,b; Jaskot 2025). From Fig. 3, we note that for a similar range in stellar mass, the galaxies in our

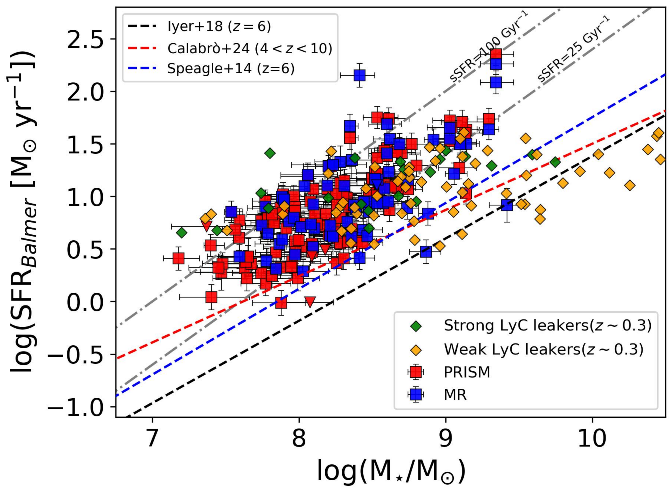

Fig. 3. Distribution of the sample in the $M_\star$–SFR plane. The red and blue squares represent the EELGs with PRISM and MR spectra, respectively. The triangle symbols are upper limits due to low Hβ S/N. The dashed black and blue lines are the main sequence of SF galaxies at $z = 6$ from Iyer et al. (2018) and Speagle et al. (2014), respectively, while the dashed red line represents the main sequence at $4 < z < 10$ from Calabrò et al. (2024b). The green (orange) diamonds are the sample of strong (weak) LyC leakers at $z \sim 0.3$ (Flury et al. 2022a; Jaskot et al. 2024a,b). The dashed-dotted lines represent constant sSFR lines.

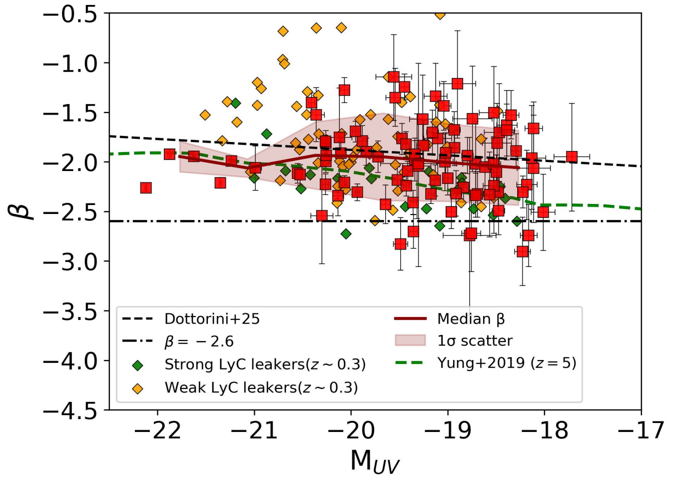

Fig. 4. Relation between $M_{\rm UV}$ and β for the sample of EELGs with PRISM spectra (red squares). The black dashed line is the relation from Dottorini et al. (2025). The dashed green line represents the predictions from SAMs at $z = 5$ (Yung et al. 2019). The red line traces the median values of β as a function of $M_{\rm UV}$, computed in bins of $M_{\rm UV}$. The shaded region corresponds to the 1σ observed scatter in the sample. Green and orange symbols are as in Fig. 3.

sample show SFRs consistent with those of the LzLCS galaxy sample, even though the latter extends to galaxies with higher stellar masses, which are mostly weak LyC leakers.

4.3. UV β slope and $M_{\rm UV}$ magnitude

The rest-frame UV continuum slope can be represented by a power-law $f_\lambda \propto \lambda^\beta$, as modelled by Calzetti et al. (1994). For the calculation of β, we considered galaxies with PRISM spectra and the fitting windows in the original definition of Calzetti et al. (1994) that exclude contamination by UV lines. We considered the rest-frame range 1309 Å $< \lambda <$ 2580 Å. We excluded shorter wavelengths due to the impact of Lyα damping wing, resulting in redder β (see Dottorini et al. 2025). We fit the windows with a linear relation $\log f_\lambda = \beta \log \lambda + q$. The fit is performed using EMCEE (Foreman-Mackey et al. 2013) with 50 walkers and 5000 steps. We adopt a flat prior on β between −4 and 0. The best-fit value is taken as the posterior median, and the uncertainty is defined by the 16th–84th percentile interval.

To account for possible residual slit losses that are not corrected by the assumption of a no wavelength-dependent correction factor, we estimated the β slope using only the photometry and checked consistency with the value estimated directly from spectra. To this aim, we considered NIRCam filters with pivot rest-frame wavelength between 1309 and 3645 Å (Balmer break). Depending on the redshift, it implies fitting between two and four filters. In Fig. F.1 we show the difference between the β calculated from the spectrum and from the photometry. We find a median difference $\Delta\beta = |\beta_{\rm spec} - \beta_{\rm photo}| = 0.36$ ($\sigma = 0.32$). This significant discrepancy arises from the limited number of filters employed in the photometric estimation. In the following analysis regarding β slope, we consider the estimation based on the spectra only in the galaxies where $\Delta\beta < 0.68$ (dashed lines in Fig. F.1), which is 75% of the sample, excluding galaxies where β is more different than 1σ the median $\Delta\beta$. For this subsample, we obtained a median value of −2.00, with a 16–84th percentile interval between −2.33 and −1.66. The mean uncertainty in the β slopes is 0.25. The estimated spectroscopic β slopes are reported in Table A.1.

Additionally, we estimated the absolute UV magnitudes ($M_{\rm UV}$) of the galaxies from the best-fit of the UV continuum of the spectra. At each step of the fitting, we computed the flux density at 1500 Å and we determined the median of the posterior distribution, while the uncertainty is given by the 16th-84th percentiles. We obtained a median $M_{\rm UV} = -19.17$ in the sample with a 16-84th percentile interval between −20.12 to −18.46.

4.4. UV continuum slopes of EELGs

In Fig. 4, we show the relation between $M_{\rm UV}$ and β slope for our sample. The median distribution of our sample (red line in Fig. 4) tends to follow the decreasing relation reported in Dottorini et al. (2025), which includes a spectroscopic sample of galaxies at similar redshifts. This decreasing trend is also predicted by semi-analytic models (SAMs) at $z = 4$–10 (Yung et al. 2019), in agreement with our results. For galaxies with $M_{\rm UV} \lesssim -21.06$, the galaxies tend to be bluer than the general population with values lower than the best-fit in Dottorini et al. (2025) for a given $M_{\rm UV}$. However, in this $M_{\rm UV}$ range, the comparison sample contains relatively few galaxies, limiting the statistical significance of this trend. For galaxies with $M_{\rm UV} \gtrsim -21.06$, we find a wide range of β slopes, bluer and redder than the general population of galaxies at similar redshifts for a given $M_{\rm UV}$. Compared to the LzLCS sample, the values of β are consistent in the range of $M_{\rm UV}$ that both samples cover, except for galaxies $M_{\rm UV} \lesssim -21.06$ where we do not find extremely red galaxies in our sample, and they are likely to be weak LyC leakers at $z \sim 0.3$. We note, however, that a subset of EELGs in our sample aligns more closely with the population of strong LyC leakers, which are typically bluer than their weaker counterparts.

We find that most of the galaxies have $\beta > -2.6$, which indicates they are not super-blue and they are above the theoretical lower limit produced by dust-free pure stellar and nebular

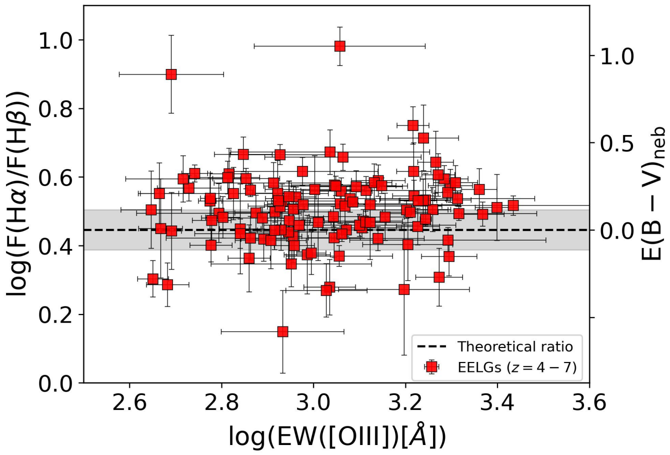

Fig. 5. Relation between Hα/Hβ ratio and EW([O III]) for the sample of EELGs (red squares). In the right y-axis, we show the corresponding $E(B-V)_{\mathrm{neb}}$. The grey shaded region corresponds to the mean error ~0.06 dex in the Hα/Hβ ratio.

continuum emission (e.g. Cullen et al. 2024). Only 7% of the sample exhibits $\beta < -2.6$; however, none of these measurements are below this value at a level greater than 1σ.

4.5. Dust reddening

The results obtained from the SED fitting indicate a wide diversity in global dust attenuation among the galaxies in our sample. The derived stellar $E(B-V)$ values span a broad range with a median value of 0.09, but reaching values from 0.009 to 0.46, highlighting significant variations in the amount of dust present within these systems. As an alternative approach to estimating dust attenuation, we use the Balmer emission lines in the subset of galaxies where both Hα and Hβ are detected. By comparing the observed Balmer decrement (Hα/Hβ) to the theoretical ratio expected for case B recombination, we derive independent estimates of dust reddening for this subsample.

To estimate the nebular $E(B-V)_{\mathrm{neb}}$, we considered the theoretical ratio Hα/Hβ = 2.79 under case B approximation for T_{e} = 15 000 K and n_{e} = 100 cm^{-3} (Pérez-Montero 2017), and the Calzetti et al. (2000) extinction law. In Fig. 5 we show the Balmer ratios as a function of EW([O III]). As can be seen, most of the galaxies in the sample show Hα/Hβ ratios higher than the theoretical value, indicating they are affected by dust reddening. In these cases, we find a median Hα/Hβ = 3.44 (σ = 0.96), which implies a median $E(B-V)_{\mathrm{neb}}$ = 0.18 (σ = 0.17). This value is slightly higher than the median stellar $E(B-V)$ = 0.09 (σ = 0.07) obtained from the SED fitting for the same subsample, but the difference is not statistically significant at the 1σ level. Previous studies have reported that the offset between nebular and stellar $E(B-V)$ decreases with increasing sSFR (Koyama et al. 2019). Interestingly, there is a subsample of galaxies that shows Hα/Hβ ratios lower than the theoretical value, taking into account the typical uncertainty of the Hα/Hβ ratios in the sample. They represent 11% of the sample where Hα and Hβ were detected. These cases can be explained by a scenario in which case B of recombination is not satisfied, and ionizing photons can escape into the IGM. Nevertheless, wavelength-dependent slit losses cannot be excluded for these galaxies.

Overall, we do not find a clear trend of dust attenuation with EW([O III]), and for a given EW([O III]), the Hα/Hβ ratios and the equivalent $E(B-V)_{\mathrm{neb}}$ are diverse. We discuss this in Sect. 7.1 in the context of the AFM model.

4.6. Gas-phase metallicity

We estimate the gas-phase metallicity using the R23 = ([OIII]$\lambda\lambda$4959,5007+[O II])/Hβ calibration presented in Sanders et al. (2024) for galaxies at z = 2.1–8.7. Given that this relation is bivalued, we also used the O32 calibration in Sanders et al. (2024). We consider the metallicity estimation to be the value from the R23 calibration that is closer to the value from the O32 calibration. We found a median log(O/H)+12 = 7.74, equivalent to 0.11 $Z_{\odot}$, but the values range from 0.03 to 0.8 $Z_{\odot}$. The same results are obtained in this approach if we use the Ne3O2 = log([Ne III]/[O II]) calibration instead of O32.

In the sample of galaxies with MR spectra, we find 8 galaxies where [O III]λ4363 Å is detected with S/N > 3. The [O III]/[O III]λ4363 Å ratios (Pérez-Montero 2017) indicate $T_{\mathrm{e}} > 1.46 \times 10^{4}$ K in this subsample. For one galaxy (ID: 81061) we also detect [O II] and Hβ, and can estimate the gas-phase metallicity with the direct method following Pérez-Montero (2017). We found a gas-phase metallicity 0.11–0.19 $Z_{\odot}$, in agreement with the median value obtained with the calibrations.

5. Are EELGs primarily AGNs or SF galaxies?

Understanding whether the ionizing radiation in galaxies arises from massive stars or AGNs is fundamental for interpreting the physical conditions within EELGs. This distinction is particularly relevant in the context of the early universe, where EELGs are considered potential analogues of the galaxies that contributed to cosmic reionization. In this section we investigate the nature of the ionizing sources in our sample to determine whether stellar populations alone can account for the observed emission or if additional sources, such as AGNs, are required.

5.1. Emission line diagnostic diagrams

5.1.1. OHNO diagram

The OHNO diagram (Backhaus et al. 2022) has been proposed as an alternative to the classical BPT diagram (Baldwin et al. 1981) for identifying narrow-line AGNs (NLAGNs) in high-redshift sources. Owing to the wavelength coverage of our spectra, this diagnostic can be applied to the EELG sample. For the subsample of galaxies where [Ne III] is detected or with upper limits, we analyse the OHNO diagram. We detect [Ne III] and [O II] in only 39 galaxies across the entire sample. For 9 additional galaxies, the detection of [O II] allows us to place an upper limit on the [Ne III]/[O II] ratio. We used this subsample, representing 25% of the total sample, for the OHNO analysis. For an additional 45 galaxies, both [Ne III] and [O II] fall within the spectral coverage, yet only upper limits are obtained for both lines. We analyse the stacked PRISM spectra of these galaxies following the methodology described in Appendix C to construct the composite spectrum.

In Fig. 6, we show the distribution of our sample in the OHNO diagram. Based on the demarcation line from Feuillet et al. (2024) calibrated for galaxies $z \leq 1.06$, only 2 galaxies are in the SF region at 3σ level, which represents 2.2% of the sample where [Ne III] and [O II] fall within the spectral

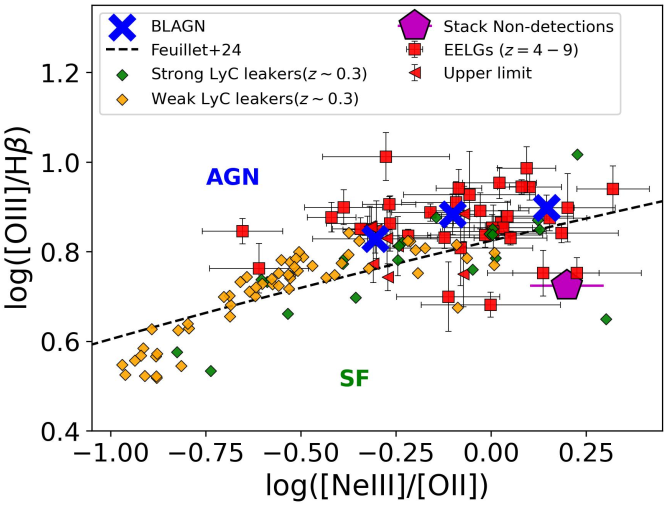

Fig. 6. OHNO diagram. The red symbols represent the sample of EELGs. The black dashed line indicates the demarcation between SF galaxies and AGNs (see labels), according to Feuillet et al. (2024). The magenta pentagon is the stacked spectrum of EELGs with undetected [Ne III] and [O II]. The blue X-symbols are EELGs classified as BLAGNs. The green and orange symbols are as in Fig. 3.

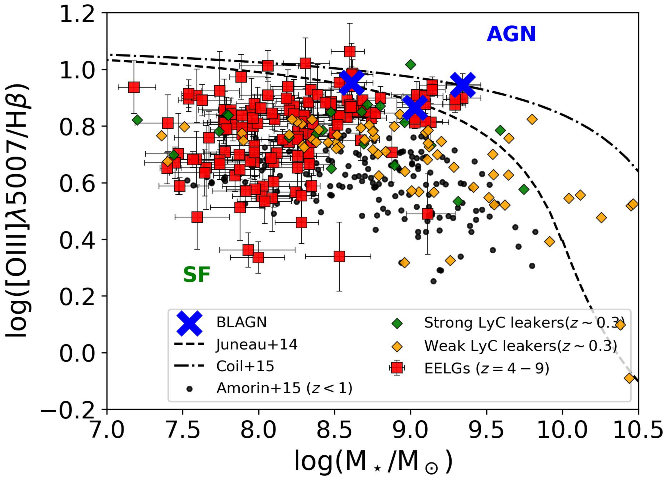

Fig. 7. MEx diagram. The red symbols represent the sample of EELGs. The dashed black line indicates the demarcation between SF galaxies and AGNs (see labels), according to Juneau et al. (2014). The dashed-dotted black line is the demarcation at $z \sim 2$ (Coil et al. 2015). The blue X-symbols are EELGs classified as BLAGNs. The black circles are EELGs up to $z \sim 1$ (Amorín et al. 2015). The green and orange symbols are as in Fig. 3.

coverage. Thirteen (18) galaxies are in the AGN region at the 3σ (2σ) level, which represents 14% (19.4%) of the same sample. 33 (28) galaxies overlap with the demarcation at the 3σ (2σ) level, suggesting that the dominant ionization source cannot be clearly identified, which represents 35.5% (30.1%) of the same sample. However, we note that this region of the diagram close to the demarcation line is also populated by the sample of low-z LyC leakers with elevated [O III]/Hβ ratios. In addition, photoionization model predictions for SF and AGNs often overlap in this region (Calabrò et al. 2023, 2024a), with the ionization parameter emerging as the main driver independently of the ionizing source (Cleri et al. 2025).

We also note that the mean log([O III]/Hβ) = 0.85 for the subsample included in the OHNO diagram is higher than the mean log([O III]/Hβ) = 0.72 measured for the remaining 48.3% of the sample where neither [Ne III] nor [O II] is detected with S/N> 3. The stacked spectrum of this latter subsample falls within the SF region (see magenta symbol in Fig. 6). This suggests that the galaxies in the OHNO diagram (red squares) represent the most extreme in terms of [O III]/Hβ ratios compared to the rest of the sample, which could alternatively be explained by harder stellar ionizing spectra and differences in gas-phase metallicity (e.g. Kewley & Dopita 2002; Bian et al. 2018), without requiring a dominant AGN contribution.

Additionally, revised versions of the OHNO diagram have demonstrated that it struggles to clearly separate AGN and SF models (e.g. Arevalo-Gonzalez et al. 2025). Recent studies have shown that the [Ne III]/[O II] ratio is a useful probe of the ionization state, but it does not effectively discriminate between excitation mechanisms, owing to the similar shapes of the ionizing SEDs at the relevant ionization potentials (e.g. Zhu et al. 2023; Flury et al. 2025a). With these caveats in mind, the estimated AGN fraction of ∼14% in our sample of EELGs should therefore be considered as a limit, as it can neither be firmly confirmed nor completely ruled out. Independent diagnostics are required to robustly assess the presence of AGNs.

5.1.2. Mass–excitation diagram

To further investigate this conclusion, we employ an alternative diagnostic. We use the mass–excitation (MEx, Juneau et al. 2011) diagram to study the ionization source in the sample of confirmed EELGs. Although the MEx diagnostic is generally less favored compared to other line-ratio methods – since it has not been thoroughly tested at high-z and is affected by systematics in stellar mass estimates (e.g. Coil et al. 2015; Cleri et al. 2023) – we retain it in our analysis because it can be applied to a large fraction of galaxies in our sample.

In Fig. 7, we present the location of our EELG sample on the MEx diagram, where they predominantly occupy the SF region, largely avoiding the AGN regime. We find that their position is consistent with the location of metal-poor starbursts with high log([O III]/Hβ) $\gtrsim$ 0.33−1.06 (mean value of 0.78). This region is populated by EELGs at $z \sim 1$ (Amorín et al. 2015) that occupy the same locus with slightly lower [O III]/Hβ ratios for galaxies with $M_\star \gtrsim 10^9\, M_\odot$. Similarly, our sample shows similar [O III]/Hβ ratios as the ones of LyC leakers at low-z at the same stellar mass range. However, we note that our sample typically spans lower stellar masses compared to the reference samples. Based on the MEx diagram, we conclude that the galaxies in our sample are predominantly powered by massive stars rather than by AGNs. This conclusion is broadly consistent with the OHNO diagram, where the stacked spectrum, representing approximately half of the sample with covered but undetected [Ne III] and [O II] lines, is consistent with ionization driven by star formation. Additionally, no galaxies in the sample show an X-ray counterpart within 2arcsec in the 800-ks Chandra imaging in EGS (Nandra et al. 2015). We note that, within the redshift range of our sample, the luminosity limit corresponds to $L_{2-10\,\mathrm{keV}} \gtrsim 10^{43}\,\mathrm{erg\,s^{-1}}$, implying that fainter AGNs may still be present but remain undetected.

Overall, the excitation properties of low-mass EELGs are predominantly consistent with ionization driven by young starbursts. However, in approximately 14% of the galaxies a NLAGN may also contribute to the ionization. This fraction should be regarded as a limit, as it cannot be robustly confirmed by our analysis and may alternatively be explained by harder stellar ionizing spectra producing similarly high line ratios.

5.2. Identification of broad-line AGN and stellar outflows

We compared our sample with the literature-based classifications of broad-line AGNs (BLAGNs) in the same field (Harikane et al. 2023; Roberts-Borsani et al. 2024; Brooks et al. 2025; Taylor et al. 2025a; Hviding et al. 2025; Kocevski et al. 2025). We found that only five galaxies (IDs: 25074, 71325, 81061, 70867, 3391) in our sample are classified as BLAGNs. To further evaluate whether there are BLAGNs in the sample, we modelled the Hα and [O III]+Hβ lines assuming two Gaussians using LiMe. For the fit, we assume that the second (broad) component has a larger velocity width than the first (narrow) component, while allowing both components to have independent systemic velocities. Given the spectral resolution of the instrument, Hα is unresolved for FWHM $<$ 940–2600 km s^{-1} (PRISM) and <240 – 371 km s^{-1} (MR), depending on redshift. For [O III], the corresponding FWHM ranges are $<$ 1045 – 4360 km s^{-1} (PRISM) and <236–410 km s^{-1} (MR). We assumed these limits for the broad component. To evaluate the necessity of the broad component, we use the Bayesian Information Criterion (BIC), which incorporates both the goodness-of-fit (χ^2) and the number of free parameters. To accept the broad emission line in the model, we require a ΔBIC > 6 (Fabozzi et al. 2014) and with S/N > 3.

In the subsample with PRISM spectra, we found that in six cases the broad component in Hα is accepted, but after a visual inspection, we found that only in two cases (IDs: 25074, 3391) is there evidence of a BLAGN in which both components have similar peak velocities ($\Delta \sim$ 100–360 km s^{-1}). Regarding the MR spectra, we found that in nine cases Hα is better modelled with a broad component, and similarly, after a visual inspection, in only four cases (IDs: 71325, 75857, 15050, 25074) is there evidence of BLAGNs ($\Delta \sim$ 4–70 km s^{-1}). Importantly, our methodology enables us to recover the galaxies previously classified as BLAGNs. We note that source 81061 is not recovered, as it is classified by Harikane et al. (2023) as a faint AGN with S/N < 3 in the broad component. Source 70867 is also not recovered because Hβ is not covered within the spectral range analysed in this paper.

The EELGs identified as BLAGNs in our sample are located in the AGN region of the OHNO diagram (blue X-symbols in Fig. 6) and in the high-mass regime of the MEx diagram (blue X-symbols in Fig. 7), consistent with an additional ionization contribution from an AGN in these galaxies. We note that only three of these sources are shown in the diagnostic diagrams, as the remaining EELGs classified as BLAGNs lack Hβ coverage in the spectra used for their classification.

Moreover, in four galaxies with accepted broad component – two observed with PRISM (ID: 45212, 47379) and two with MR (IDs: 75511, 28312) – the broad component is velocity-shifted (Δ > 360 km s^{-1} for PRISM and Δ > 90 km s^{-1} for MR) relative to the narrow component, which may indicate an outflow rather than a BLAGN. In all the above cases, [O III] modelling reveals the absence of a broad component.

We identify a subsample of five galaxies (IDs: 66855, 75478, 78647, 47504, 59920) with MR spectra where Hα is not covered (partially in ID: 75478) and where a broad [O III] component is accepted, which may indicate the presence of outflows. However, no unambiguous outflow signatures are detected in the EELG sample. Outflows may not be ongoing at the time of observation but could have previously cleared dust, as suggested by the AFM. Alternatively, the lack of detection of outflows could be due to the limited spectral resolution of the PRISM and MR data; confirming their presence would require follow-up with higher-resolution spectroscopy and improved sensitivity.

Based on this Gaussian modelling, the lines are well described by a single Gaussian, indicating that while BLAGNs may be present, they do not dominate the Balmer line emission. Given the small fraction of BLAGNs in our sample, we do not remove them from the analysis. Their minimal contribution (<4%) is unlikely to significantly impact the statistical properties or overall trends of the EELG population. We conclude that massive stars are the dominant source of ionization in EELGs without significant fractions of BLAGNs, although about 14% of the galaxies are still consistent with a NLAGN contribution based on diagnostic diagrams.

6. The contribution of EELGs to cosmic reionization

Several studies indicate that SF galaxies may be the primary drivers of cosmic reionization (e.g. Finkelstein et al. 2019; Yung et al. 2020a; Robertson 2022). However, the efficiency with which these galaxies produced and leaked LyC photons into the IGM is still poorly constrained. Due to their low metallicities, compact morphologies, and intense radiation fields, EELGs emerged as promising key players in cosmic reionization (e.g. Begley et al. 2025), given that they could have large $\xi_{\rm ion}$ and potentially elevated fesc$_{\rm LyC}$, both of which are crucial parameters in determining their contribution to reionization. In this section we study these two parameters in EELGs to understand their role during the EoR.

6.1. Ionizing photon production efficiency

Ionizing photon production efficiency is a key parameter that quantifies the number of hydrogen-ionizing photons produced per unit of UV luminosity. SAMs predict that, due to a strong metallicity dependency, UV-faint, low-mass galaxies have $\xi_{\rm ion}$ values that are up to a factor of 2 higher than those of more massive galaxies, with the efficiency further enhanced at higher sSFRs (Yung et al. 2020b). We estimated $\xi_{\rm ion}$ following Llerena et al. (2025), with $\xi_{\rm ion} = \dfrac{\rm N(H^0)}{\rm L_{UV}}$, where N(H^0) is the ionizing photon rate in units s^{-1} and $L_{\rm UV}$ is the UV luminosity density in units of erg s^{-1} Hz^{-1} at rest-frame 1500 ÅWe estimate N(H^0) using the dust-corrected Hα luminosity as $L({\rm H}\alpha)[{\rm erg\,s^{-1}}] = 1.36 \times 10^{-12} N(H^0)\,[{\rm s^{-1}}]$, which was derived from Leitherer & Heckman (1995) assuming no ionizing photons escape from the galaxy and case B recombination. For fesc$_{\rm LyC}$ > 0, $\xi_{\rm ion}$ scales by a factor 1/(1 – fesc$_{\rm LyC}$).

In Fig. 8, we show the relation between EW([O III]) and $\xi_{\rm ion}$. This relation arises because large EWs are typically linked to young, metal-poor stellar populations, which are expected to produce copious amounts of hydrogen-ionizing photons (e.g. Chevallard et al. 2018). We found a median log($\xi_{\rm ion}$ [Hz erg^{-1}]) = 25.37, with a 16–84th percentile interval between 25.19 and 25.50 (Table 2). The median $\xi_{\rm ion}$ for the sample is higher than the median log($\xi_{\rm ion}$ [Hz erg^{-1}]) = 25.22 found for the general population of star-forming galaxies at similar redshift (Llerena et al. 2025) and also predicted from SAMs at z = 6–8 in the same stellar mass range of the sample with Bruzual & Charlot (2003) models (Yung et al. 2020b). Our sample follows the relations found in a wide range of redshifts (e.g.

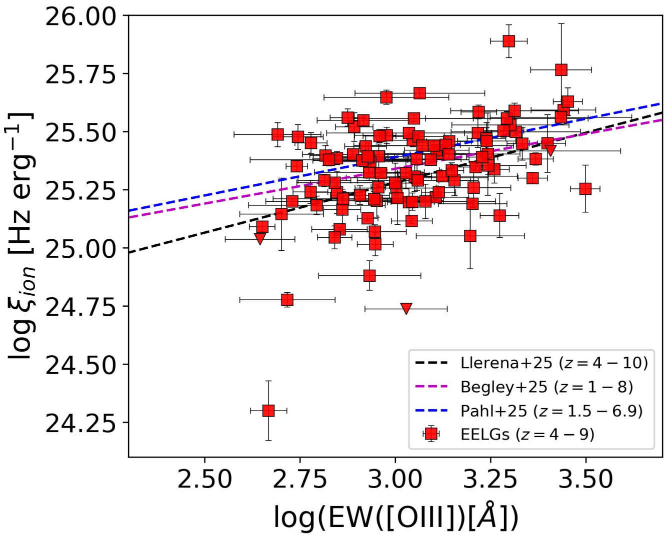

Fig. 8. Relation between EW([O III]) and $\xi_{\rm ion}$. The dashed black, magenta, and blue lines are the relations from Llerena et al. (2025), Begley et al. (2026), and Pahl et al. (2026), respectively.

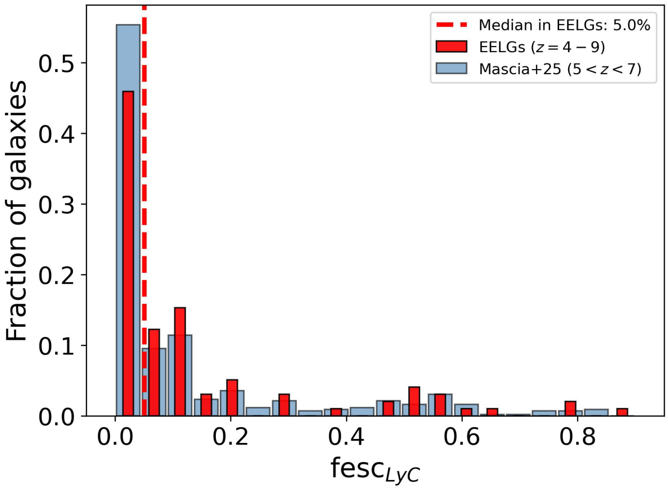

Fig. 9. Distribution of $\rm fesc_{LyC}$ in the sample of EELGs. The dashed red line is the median of the distribution. The blue histogram is the $\rm fesc_{LyC}$ distribution in galaxies at $5 < z < 7$ from Mascia et al. (2025).

Llerena et al. 2025; Begley et al. 2026; Pahl et al. 2026) with an increasing $\xi_{\rm ion}$ with increasing EW([O III]). We note that even in the most extreme EW([O III]), the $\xi_{\rm ion}$ values do not reach the theoretical limits of $\log(\xi_{\rm ion}\,[\rm Hz\,erg^{-1}]) = 26$ expected for young metal-poor stellar populations (Raiter et al. 2010; Maseda et al. 2020) and from simulations of PopIII populations (Lecroq et al. 2025). Therefore, EELGs are efficient producers of ionizing photons, although they are not the most efficient ones, as they do not reach the maximum theoretical values of $\xi_{\rm ion}$.

6.2. The escape of LyC photons

Given that at the redshift of our EELGs the $\rm fesc_{LyC}$ cannot be measured directly due to the IGM opacity, we inferred it using models based on multivariate indirect diagnostics (Jaskot et al. 2024a,b). Results of the LzLCS survey indicate that $\rm fesc_{LyC}$ correlates with several galaxy properties, including dust attenuation, $\rm fesc_{Ly\alpha}$, and the O32 ratio (e.g. Flury et al. 2022b; Chisholm et al. 2022; Saldana-Lopez et al. 2022; Xu et al. 2023). However, these correlations exhibit significant scatter, suggesting that no single observable can reliably predict $\rm fesc_{LyC}$ on its own and that a more accurate description requires a combination of multiple galaxy properties.

To address these limitations, Jaskot et al. (2024a,b) applied survival analysis techniques, in particular Cox models. These semi-parametric models estimate the probability of detecting $\rm fesc_{LyC}$ as a function of multiple galaxy properties, providing a more robust framework for predicting $\rm fesc_{LyC}$ compared to traditional methods such as linear regression. The performance of the Cox models is quantified using the concordance index (C), a goodness-of-fit metric that ranges from 0 (perfect disagreement) to 1 (perfect concordance). These Cox models were subsequently recalibrated by Mascia et al. (2025) using a subset of LzLCS galaxies (Flury et al. 2022a) selected to resemble the physical properties of high-redshift sources, enabling more reliable predictions of $\rm fesc_{LyC}$ during the EoR. In this work, we adopt the revised ELG–O32 and revised ELG–EW Cox models from Mascia et al. (2025), which achieve concordance indices of $C = 0.83$ and $C = 0.79$, respectively.

First, we consider the revised ELG-O32 Model which estimates $\rm fesc_{LyC}$ from $M_{\rm UV}$, stellar mass, $E(B-V)$, and O32 ratio. In the cases where O32 is not determined in our sources due to low S/N of [O II] or the wavelength coverage, we consider the revised ELG-EW Model, which depends on the same indirect parameters but uses EW([O III]+Hβ) instead of O32. In our sample, O32 values range from 0.44 to 1.35, with an average of 0.89, exceeding the O32 = 0.69 threshold commonly observed in strong leakers at low-z (Flury et al. 2022b). Notably, among the 46 galaxies with detected [O II] emission, 34 (74%) exhibit O32 ratios above 0.69. We employed a Monte Carlo approach, perturbing the model parameters according to their uncertainties to generate 1000 random realizations. From the resulting distributions of $\rm fesc_{LyC}$, we report the median as the best estimate (reported in Table A.1) and the 16th–84th percentiles as their uncertainties.

In Fig. 9, we show the distribution of $\rm fesc_{LyC}$ in the EELG sample. We find a median (mean) value of $\rm fesc_{LyC}$ = 5% (14.5%) with a 16–84th percentile interval from 0.8 to 29% (Table 2). In 51% of the sample, we find $\rm fesc_{LyC} >$ 5% which indicates that half of EELGs are strong LyC leakers but they are not a dominant population since half of the sample are weak LyC leakers. The median value is consistent with the $\rm fesc_{LyC}$ predicted by the AFM at $z \sim 5$–6 (Ferrara et al. 2025) and slightly higher than the median value of 4% from inferred $\rm fesc_{LyC}$ in a sample of 436 galaxies at z = 5–7 with a wide range of EW([O III]+Hβ) and using the same methodology (Mascia et al. 2025). This suggests that, although half EELGs exhibit elevated $\rm fesc_{LyC}$, half are unlikely to be strong LyC leakers. Moreover, the $\rm fesc_{LyC}$ distribution in EELGs closely follows that of the general galaxy population at similar redshifts (Mascia et al. 2025), not necessarily selected as EELGs, indicating that EELGs are not particularly more efficient LyC leakers than other galaxies at comparable epochs.

6.3. The escape of Lyα photons

Lyα emission is considered one of the key proxy for LyC escape. At low and intermediate-z, several Lyα properties (like its EW or the separation between blue and red peaks) correlate with LyC leakage, albeit with significant scatter (Marchi et al. 2017;

Table 2. Median values and 16–84th percentile intervals for the different parameters analysed in Sects. 6 and 7.

	Median	Interval	ρ [a]	$\rho_{\rm partial}$ [a]
$\log(\xi_{\rm ion}$ [Hz erg^{-1}])	25.37	(25.19, 25.50)	–	–
$\mathrm{fesc_{LyC}}$	5%	(0.8%, 29%)	–	–
$\mathrm{fesc_{LyC}}$ *	5.1%	(1.3%, 43.5%)	–	–
$\mathrm{fesc_{LyC}}$ †	11.8%	(1.2%, 40.5%)	–	–
$\mathrm{fesc_{LyC}}$ ‡	1.3%	(0.44%, 3.4%)	–	–
$\mathrm{fesc_{Ly\alpha}}$ §	14.6%	(6%, 30%)	–	–
sSFR [Gyr^{-1}]	43	(24, 103)	0.64	0.42
$r_{\rm opt}$ [kpc]	0.49	(0.19, 0.86)	−0.37	−0.09
$\Sigma_{\rm SFR}$ [$M_\odot$ yr^{-1} kpc^{-2}]	10.7	(1.9, 56)	0.50	0.41
$\log(M_{\rm gas}/M_\odot)$	9.28	(8.95, 9.71)	–	–
$f_{\rm gas}$	87%	(80%, 93%)	–	–
$\log(\mathrm{SFR_{3\,Myr}/SFR_{100\,Myr}})$	1.16	(0.84, 1.59)	0.46	0

Notes. [a]We also summarize the correlation coefficientes, ρ, for each parameter with EW([O III]) shown in Sect. 7 and the partial correlation coefficientes, $\rho_{\rm partial}$, shown in Sect. 7.5. We note that these correlations are valid only in the range of high EWs and z covered by our sample ($2.6 \lesssim \log(\mathrm{EW([O\,III])}) \lesssim 3.6$). *For EELGs with sSFR > 25 Gyr^{-1}. †For EELGs with sSFR > 25 Gyr^{-1} and $r_{\rm opt}$ < 200 pc. ‡For EELGs with sSFR < 25 Gyr^{-1}. §For the sample of LAEs at z < 7 in our sample.

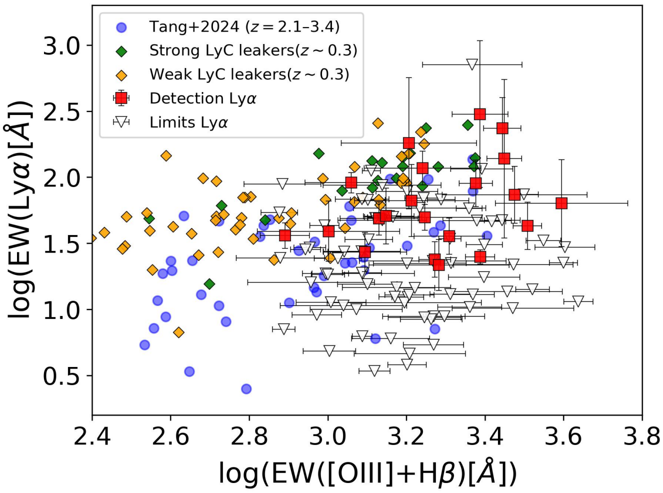

Fig. 10. Relation between the EW([OIII]+Hβ) and EW(Lyα). The red squares are the sample of EELGs with detected Lyα, while the white triangles are upper limits. The blue circles are the sample from Tang et al. (2024). The green and orange symbols are as in Fig. 3.

Izotov et al. 2020; Flury et al. 2022b). In this section we investigate the Lyα properties in the sample of EELGs to assess whether they are consistent with the modest inferred $\mathrm{fesc_{LyC}}$ for these galaxies. First, we focus on the EW(Lyα). In Fig. 10 we show the relation between EW([O III]+Hβ) and EW(Lyα). For this figure, we considered the subsample of LAEs (red squares) and the non-LAEs subsample with upper limits (white triangles). In the subsample of LAEs, EW(Lyα) ranges from 21 to 300 Å with a median value of 50 ÅÅ subsample of EELGs show high EW(Lyα) $\gtrsim$ 100 Å (24% of the subsample of LAEs).

We compared our results with previous works at z = 2.1–3.4 (Tang et al. 2024), and we find that our sample of LAEs follows the trend of increasing EW(Lyα) with increasing EW([O III]+Hβ), showing a moderate correlation (ρ = 0.62, $p = 7\times10^{-8}$) when including the sample at intermediate-z. Our sample covers the region of more extreme EW([O III]+Hβ) and consequently higher EW(Lyα) compared to LAEs at intermediate-z (Tang et al. 2024). This increasing trend is also observed in low-z LyC leakers. However, we note that Lyα emission is not detected in all EELGs of the sample, with only 18% classified as LAEs. This indicates that a high EW([O III]+Hβ) does not necessarily imply a high EW(Lyα), which is consistent with a diversity in the properties of EELGs that facilitate the escape of Lyα photons. This supports a mixed population of weak and strong LyC leakers, since the escape fraction of Lyα photons ($\mathrm{fesc_{Ly\alpha}}$) has been shown to correlate with $\mathrm{fesc_{LyC}}$ as both processes are facilitated by low neutral hydrogen column densities and porous ISM geometries (e.g. Verhamme et al. 2015; Begley et al. 2024).

To quantify $\mathrm{fesc_{Ly\alpha}}$ in our sample, we use the flux ratio between Lyα and dust-corrected Hα. To this aim, we considered the theoretical ratio Lyα/Hα = 8.7 (Hayes 2015). We restrict our analysis to galaxies with z < 7, where the EGS field has recently been reported to be largely ionized (e.g. Napolitano et al. 2026), to minimize the impact of neutral IGM on Lyα emission. In our LAE sample, $\mathrm{fesc_{Ly\alpha}}$ spans 2%–55%, with a median of 14.7% with a 16-84th percentile interval from 6% to 30% (Table 2), consistent with the median $\mathrm{fesc_{Ly\alpha}}$ of 18% in the low-z LyC leakers. Considering also the upper limits in the non-LAE subsample, which in most cases are below 5%, we conclude that the average escape of Lyα in EELG is modest. This is consistent with results from samples of LAEs at $z \approx 6$, where it has been found that, although these systems can reach high $\xi_{\rm ion}$ values, their $\mathrm{fesc_{Ly\alpha}}$ is typically $\lesssim$10%, with bluer and UV-fainter LAEs exhibiting higher $\mathrm{fesc_{Ly\alpha}}$ (Ning et al. 2023).

Overall, although some EELGs appear to exhibit high $\mathrm{fesc_{Ly\alpha}}$ and $\mathrm{fesc_{LyC}}$, not all are likely to be strong leakers. Only 16% of the sample at z < 7 shows $\mathrm{fesc_{Ly\alpha}}$ and $\mathrm{fesc_{LyC}}$ >5%. This is supported by the absence of Lyα emission in several cases and the fact that the median inferred $\mathrm{fesc_{LyC}}$ is not particularly elevated. Coupled with the fact that the EELGs show moderately elevated $\xi_{\rm ion}$ values, this highlights the need for a proper estimation of their fractional contribution to the cosmic reionization.

6.4. Fractional contribution to the ionizing budget

In this section we assess the median fractional contribution of the population represented by our sample to the total ionizing emissivity ($\dot{n}_{\rm ion}^{\rm SF}$) of SF galaxies, defined as the comoving density of LyC photons produced per unit time that are available to ionize hydrogen in the IGM and expressed as $\dot{n}_{\rm ion}^{\rm SF} = \rho_{\rm UV}^{\rm SF}\,\xi_{\rm ion}^{\rm SF}\,\mathrm{fesc_{LyC}^{SF}}$, where $\rho_{\rm UV}^{\rm SF}$ is the comoving total UV luminosity density of SF galaxies. On the other hand, the total ionizing emissivity attributable to EELGs can be expressed as $\dot{n}_{\rm ion}^{\rm EELG} = \rho_{\rm UV}^{\rm EELG}\,\xi_{\rm ion}^{\rm EELG}\,\mathrm{fesc_{LyC}^{EELG}}$.

A robust determination of the fractional contribution $\dot{n}_{\rm ion}^{\rm EELG}/\dot{n}_{\rm ion}^{\rm SF}$ requires a full characterization of $\rho_{\rm UV}^{\rm EELG}$, which is beyond the scope of this work. Instead, we adopt a set of simplifying assumptions to estimate a representative median fractional contribution. Recent studies have found that galaxies with EW([O III]+Hβ) > 1500 Å represent a fraction of ~28% of the galaxy population at z ~ 7–8 (Endsley et al. 2023). However, Endsley et al. (2024) showed that bright ($-22 < M_{\rm UV} < -19.5$), intermediate ($-19.5 < M_{\rm UV} < -18$) and faint ($-18 < M_{\rm UV} < -16.5$) EELGs at z ~ 6–9 exhibit distinct EELG fractions ($f_{\rm EELG}$) decreasing systematically toward fainter UV magnitudes. We estimate these fractions in our photometric parent sample and find a similar trend, with galaxies with EW([O III]+Hβ) > 680 Å representing $f_{\rm EELG}$ = 42%, 27%, 25%

of bright, intermediate, and faint UV galaxies at $z \sim 6$, respectively. Very-faint ($-16.5 < \mathrm{M_{UV}} < -13$) galaxies are also crucial for determining $\dot{n}_{\mathrm{ion}}^{\mathrm{SF}}$, since they are expected to contribute ~60–65% of the total budget (e.g. Mascia et al. 2024). However, our sample does not probe this very faint regime where we must rely on extrapolation. Under the assumption of a linear decline in the EELG fraction, we infer a median $f_{\mathrm{EELG}} = 13\%$ in this range of UV magnitudes.

We compute $\dot{n}_{\mathrm{ion}}^{\mathrm{SF}}$ in the same four bins of UV luminosity. We adopt the UV luminosity function at $z \sim 6$ from Bouwens et al. (2021). For $\xi_{\mathrm{ion}}^{\mathrm{SF}}$, we use the median $\log(\xi_{\mathrm{ion}}\ [\mathrm{Hz\ erg^{-1}}])$ values in each UV bin, based on the ξ_{ion}–M_{UV} relation presented in Llerena et al. (2025). For the escape fraction, we adopt the median $\mathrm{fesc_{LyC}} = 4\%$ at $z \sim 5-7$ from Mascia et al. (2025), inferred using a methodology consistent with that adopted in this work. This yields $\log(\dot{n}_{\mathrm{ion}}^{\mathrm{SF}}[\mathrm{s^{-1}\ Mpc^{-3}}]) = 50.1^{+0.13}_{-0.19}$, consistent with the emissivity required to maintain reionization at $z = 6$ (Madau et al. 1999). Approximately 72% of the SF budget is produced by very-faint sources, partially driven by the elevated extrapolated median $\log(\xi_{\mathrm{ion}}\ [\mathrm{Hz\ erg^{-1}}]) = 25.95$, which is consistent with measurements in small samples of very-faint sources in lensed fields at $z \sim 6$ (e.g. Atek et al. 2024; Asada et al. 2026), as well as in individual galaxies at similar redshifts with $M_{\mathrm{UV}} \gtrsim -12$, which show elevated ξ_{ion} with both high (e.g. Vanzella et al. 2024) and low (e.g. Vanzella et al. 2023) EW([O III]).

To compute $\dot{n}_{\mathrm{ion}}^{\mathrm{EELG}}$, we assume $\rho_{\mathrm{UV}}^{\mathrm{EELG}} = f_{\mathrm{EELG}}\ \rho_{\mathrm{UV}}^{\mathrm{SF}}$. For $\xi_{\mathrm{ion}}^{\mathrm{EELG}}$, we found a median offset of 0.14 dex in our sample with respect to the ξ_{ion}–M_{UV} relation presented in Llerena et al. (2025). Assuming these median offsets for the median $\xi_{\mathrm{ion}}^{\mathrm{SF}}$, and the median $\mathrm{fesc_{LyC}} = 5\%$ in our sample, we estimate that EELGs contribute $27^{+13}_{-11}\%$ of $\dot{n}_{\mathrm{ion}}^{\mathrm{SF}}$ when summing all contributions from bright to very-faint sources. Therefore, EELGs with large EW([O III]+Hβ) play a non-negligible role in the total ionizing photon budget of SF galaxies.

In our analysis, the value of $\dot{n}_{\mathrm{ion}}^{\mathrm{EELG}}/\dot{n}_{\mathrm{ion}}^{\mathrm{SF}}$ is driven by the fact that at very-faint UV luminosities, where the bulk of the budget is produced, the fractional contribution of EELGs is small (~18%). Indeed, assuming $f_{\mathrm{EELG}} = 0$ in the very-faint regime yields $\dot{n}_{\mathrm{ion}}^{\mathrm{EELG}}/\dot{n}_{\mathrm{ion}}^{\mathrm{SF}} = 13\%$, which can be interpreted as the minimum median fractional contribution of EELGs. We note that our sample at faint and very-faint UV luminosities is highly incomplete, comprising only four galaxies and none, respectively, highlighting the need for a more comprehensive characterization of ξ_{ion} and $\mathrm{fesc_{LyC}}$ in this regime for both SF galaxies and EELGs given that the median properties of very-faint sources are largely uncertain. Moreover, we note that the fraction f_{EELG} of galaxies with EW([O III]) > 750 Å has been shown to increase with redshift (Boyett et al. 2024), which may further enhance the fractional contribution of EELGs at earlier epochs. In addition, as discussed in Sect. 7.2, the LyC escape fraction may be elevated in specific subpopulations of EELGs characterized by compact star-forming regions, potentially increasing their contribution to cosmic reionization.

7. The drivers of high EWs

In this section we explore the potential physical properties responsible for the elevated EW([O III]) observed in our sample. We examine various properties that could contribute to this enhancement. Furthermore, we place our findings within the broader context of galaxies with SE star-formation. A summary of the results of this section are reported in Table 2, including the correlation parameters of the relations with EW([O III]).

7.1. Elevated and compact star formation

In the top-left panel in Fig. 11, we show a strong correlation ($\rho = 0.64$, $p \sim 0$) between EW([O III]) and sSFR, where the most extreme emitters show elevated sSFR. A similar trend is found with EW(Hβ). While our sample is limited to high-EW galaxies, this increasing trend has also been reported for lower-EW galaxies at $0.1 < z < 0.94$ (Amorín et al. 2015). Our sample shows more extreme EWs and sSFRs than low-z LyC leakers, more consistent with the subsample of strong leakers. The elevated sSFRs seem to be a potential driver of the high EWs observed in the sample. In particular, the median sSFR in the sample is 43 Gyr^{-1}, with 16-84th percentile interval from 24 to 103 Gyr^{-1}, and most of the galaxies (80%) show sSFR > 25 Gyr^{-1} with high EWs. This is the threshold for a galaxy to develop a radiation-driven outflow, ejecting both dust and gas from the system, assuming that the source is sufficiently compact (effective radius $\lesssim$200 pc, Ferrara 2024). Our results imply a fraction of 19% super-Eddington galaxies (only assuming the threshold in sSFRs) in the total population of SF galaxies at $z \sim 6$, based on the parent sample defined for the photometric selection of EELGs, which contains 738 galaxies within $5.5 < z_{\mathrm{phot}} < 6.5$.

We also analyse a possible relation between EW and galaxy compactness. To measure the rest-frame UV (r_{UV}) and optical (r_{opt}) effective radii of the galaxies in our sample, we use the Galfit catalogue v2.0 from the CEERS collaboration (McGrath et al. 2026). Galfit (Peng et al. 2002, 2010) was run for sources with F356W < 28.5 mag using background-subtracted mosaics. To determine r_{opt}, we considered the effective radius in the filter F277W, F356W, and F444W for galaxies at $z < 6$, $6 < z < 8$, and $z > 8$, respectively. For Galfit modelling, we restricted our analysis to galaxies with a good quality flag (so-called Flag = 0) in the corresponding filter, representing 66% of the total sample. The r_{opt} are reported in Table A.1. For this subsample, we also determined r_{UV} considering the effective radius in the filter F115W and F150W for galaxies at $z < 6$ and $z > 6$, respectively. We found a median $r_{\mathrm{UV}}/r_{\mathrm{opt}} = 0.96$.

In the top-right panel in Fig. 11 we show the relation between r_{opt} and EW([O III]), which are moderately anti-correlated ($\rho = -0.37$, $p = 1.2\times10^{-4}$), with galaxies with the most extreme EWs showing the most compact sizes. The median r_{opt} is 0.49 kpc with values from 104 pc to 3.70 kpc, indicating that EELGs tend to be compact, which is a necessary condition for the development of radiation-driven outflows according to the AFM model. In particular, we note that 17% of the EELGs have $r_{\mathrm{opt}} < 200$ pc. Compared to extreme emitters at $z = 1.3-3.7$ (Tang et al. 2022), our galaxies are more extreme in terms of EWs and r_{opt}, but they follow the trend observed at lower redshifts. We verified that the median r_{opt} of all sources in the Galfit catalogue within the same redshift range and quality flag is 0.69 kpc, indicating that EELGs are, on average, more compact than galaxies at similar redshifts. In addition, we note that all low-z strong LyC leakers have sizes below the median size of high-z galaxies, suggesting that compact sizes may not only drive the high EWs observed in the sample but also facilitate the escape of ionizing radiation.

7.2. LyC escape in EELGs with SE activity

We discuss our results in Sects. 6.2 and 7.1 in the context of the AFM model. The fraction of SE galaxies in the parent sample (19%) agrees very well with the expected fraction of 22% predicted by AFM at $z \sim 6$ (Ferrara et al. 2025). The small difference may result from the approximate comparison between

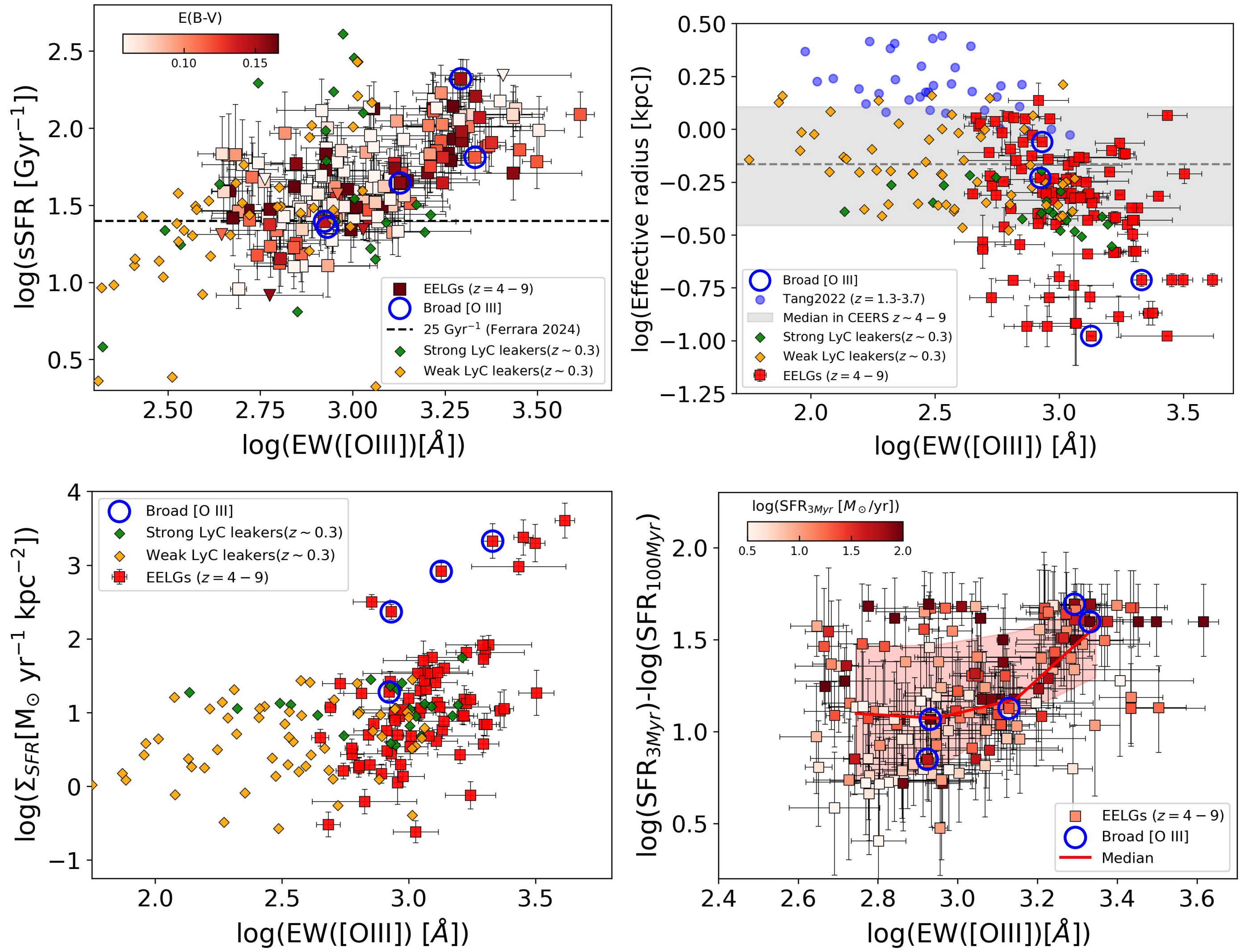

Fig. 11. Relation between EW([O III]). *Top left*: sSFR. The symbols are colour-coded by $E(B-V)$ from SED fitting. The triangle symbols are upper limits due to low Hβ S/N. The dashed line is the threshold for super-Eddington galaxies (Ferrara 2024). *Top right*: $r_{\rm opt}$. The blue circles are EELGs at intermediate-z (Tang et al. 2022). The horizontal dashed grey line is the median $r_{\rm opt}$ in CEERS in the same redshift range. The shaded region indicates the 16th–84th percentile range. *Bottom left*: $\Sigma_{\rm SFR}$. *Bottom right*: SFR$_{3\,\rm Myr}$/SFR$_{100\,\rm Myr}$, as a proxy of the burstiness. The galaxies in the sample are colour-coded by the average SFR in the last 3Myr. The red line traces the median values of burstiness computed in bins of EW, while the shaded region is the 16th-and 84th percentiles. In all panels, green and orange symbols are as in Fig. 3. Open blue circles mark the position of EELGs identified in Sect. 5.2 with evidence of broad [O III], suggesting the presence of stellar outflows.

spectroscopic and photometric samples, or from some SE galaxies missed due to extremely low metallicities, which prevent them from being classified as EELGs (e.g. Laseter et al. 2025).

Galaxies in our sample also show relatively low and moderate $E(B-V)$ (top-left panel in Fig. 11 and Table 1) as expected by AFM, with the level of dust clearing depending on the evolutionary phase of the outflow, leading to reduced attenuation at later stages. Consistent with this picture, the small subsample of five EELGs showing evidence of broad [O III] emission (open blue circles in Fig. 11), likely tracing stellar-driven outflows as discussed in Sect. 5.2, exhibits sSFR values above the threshold for SE activity and compact sizes, suggesting a link between enhanced star formation, radiation-driven outflows, and the physical conditions that may facilitate LyC escape.

Interestingly, as shown in Fig. 12, for a given sSFR the inferred fesc$_{\rm LyC}$ values are diverse, with SE galaxies exhibiting both low and high fesc$_{\rm LyC}$. We also note that all EELGs with highly efficient fesc$_{\rm LyC}$ > 20% show sSFR > 25 Gyr^{-1}, suggesting that SE star-formation may be a necessary, though not sufficient, condition for high LyC escape. In addition, the median fesc$_{\rm LyC}$ of galaxies with sSFRs > 25 Gyr^{-1} is 5.1% (16–84th percentile interval: 1.3%–43.5%), while for galaxies below is 1.3% (16–84th percentile interval: 0.44%–3.4%), which suggests that elevated sSFRs enhance fesc$_{\rm LyC}$, in agreement with the AFM models.

Additionally, an enhancement in fesc$_{\rm LyC}$ is observed in galaxies with sSFR > 25 Gyr^{-1} which also have $r_{\rm opt}$ < 200 pc (open squares in Fig. 12), representing 15% of EELGs, with a median fesc$_{\rm LyC}$ = 11.8% (16–84th percentile interval: 1.2%–40.5%), while galaxies with sSFR > 25 Gyr^{-1} and $r_{\rm opt}$ > 200 pc, representing 68% of EELGs, show a median fesc$_{\rm LyC}$ = 5.2% (16–84th percentile interval: 1.4%–48.4%). This apparent enhancement is consistent with results from low-z LyC leakers, which suggest that compactness is linked to increased feedback efficiency when star formation is spatially concentrated (Flury et al. 2022b). In such compact SF regions, feedback can efficiently

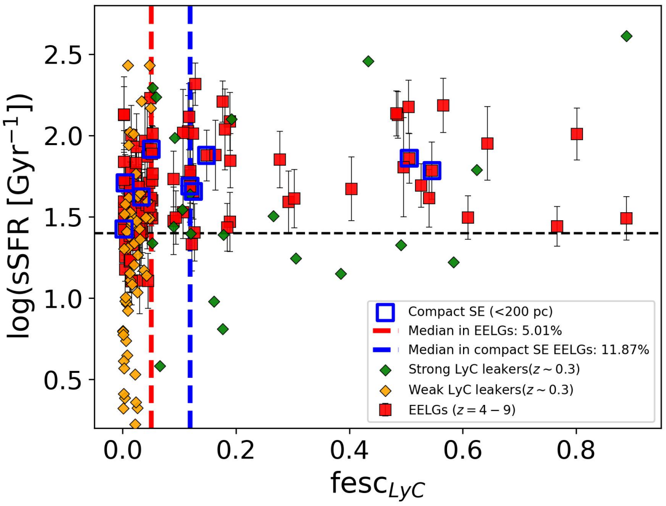

Fig. 12. Inferred fesc$_{\rm LyC}$ vs. sSFR in the sample of EELGs (red squares). The horizontal dashed black line represents the 25 Gyr^{-1} threshold for SE regime. The blue open squares mark the position of galaxies with compact (<200 pc) SE activity. The dashed red and blue vertical lines represent the median fesc$_{\rm LyC}$ for the entire sample and compact SE, respectively. The green and orange symbols are as in Fig. 3.

deplete or disrupt the surrounding gas, enabling LyC photons to escape the local H II regions, propagate through the more diffuse ISM, and potentially leak into the IGM.

7.3. SFR surface density

Given that these systems show compact effective radii, we expect they host high SFR surface densities $\left(\Sigma_{\rm SFR} = \dfrac{\rm SFR}{2\pi r_{\rm UV}^2}\right)$. We derived this parameter for this sample, and found a median value of 10.7 $M_\odot$ yr^{-1} kpc^{-2}, with the 16–84th percentile interval between 1.9 and 56 $M_\odot$ yr^{-1} kpc^{-2}. This range is consistent with the high $\Sigma_{\rm SFR}$ measured in low-z LyC leakers, as shown in the bottom-left panel in Fig. 11. Also, the median value in the sample is consistent with the threshold of 10 $M_\odot$ yr^{-1} kpc^{-2} above which nearly all strong LyC leakers appear in the LzLCS survey (Flury et al. 2022b), suggesting a population of strong and weak LyC leakers in our EELG sample. However, we note that 11% of the sample show $\Sigma_{\rm SFR} > 100\,M_\odot$ yr^{-1} kpc^{-2}, with a subsample of them showing evidence of broad [O III] emission. Assuming the Kennicutt-Schmidt law (Kennicutt & Evans 2012), this implies a high total baryonic mass of the gas ($M_{\rm gas}$) involved in star formation within the effective radius, with a median value of $\log(M_{\rm gas}/M_\odot) = 9.28$ (16–86th percentiles: 8.95 and 9.71). Given the low stellar masses of these systems, such large $M_{\rm gas}$ values correspond to high gas fractions $\left(f_{\rm gas} = \dfrac{M_{\rm gas}}{M_{\rm gas} + {\rm M}_\star}\right)$ ranging from 33% to 98%, with a median value of 87%. These values are consistent with those estimated using similar methods for EELGs at $z = 0.1{-}0.9$ (Calabrò et al. 2017). In the bottom-left panel in Fig. 11, we show that $\Sigma_{\rm SFR}$ and EW([O III]) are moderately correlated ($\rho = 0.50$, $p = 4 \times 10^{-6}$), which appears slightly stronger than the correlation with the effective radius. This suggests that the strength of the [O III] emission is more closely linked to the intensity of compact star formation than to the overall size of the galaxy.

Overall, elevated sSFRs and compact star-formation activity appear to drive high EWs. The high sSFRs and small effective radii, which place them in the super-Eddington regime, lead to an enhancement of fesc$_{\rm LyC}$ with moderate and low $E(B-V)$ values.

7.4. Burstiness in EELGs

Bursty star formation is a key characteristic of EELGs. Analogues of high-z EELGs in the local universe, such as compact SF galaxies with small linear radii of a few kiloparsecs in the Sloan Digital Sky Survey, exhibit highly bursty star formation histories, resulting in rapid luminosity variations on Myr timescales (Izotov et al. 2016). Furthermore, Flury et al. (2025b) shows that a two-stage star-formation burst, with an initial phase that generates feedback via stellar winds and supernovae and a second phase that produces LyC photons, is necessary for strong LyC escape by providing both mechanical and ionizing feedback capable of redistributing or removing LyC-obscuring gas and dust. These findings underscore the relevance of burstiness for EELGs, particularly concerning their potential to leak LyC photons.

In this section we analyse the SFH of EELGs based on the SED model. Given that SFHs indicate EELGs are experiencing a burst over the last 3 Myr, we investigate their burstiness by comparing this timescale with a longer period of 100 Myr. For this analysis, we consider the SFRs obtained from the non-parametric SED modelling. We estimated the average SFR in the last 3 Myr and in the last 100 Myr, and the uncertainties are estimated from the average of the 16th and 84th percentiles of the SFR distribution. We calculated the burstiness by the ratio SFR$_{3\,\rm Myr}$/SFR$_{100\,\rm Myr}$ which is shown in the bottom-right panel in Fig. 11. We note that all EELGs have SFR$_{3\,\rm Myr}$ > SFR$_{100\,\rm Myr}$ and exhibit a median $\log({\rm SFR}_{3\,\rm Myr}) - \log({\rm SFR}_{100\,\rm Myr}) = 1.16$ ($\sigma = 0.31$), which is an increase in SFR by a factor of 14.6 over the last 3 Myr, indicating that they are young starbursts. This level of burstiness implies that, on average, 36% of the stellar mass in EELGs is assembled within the last 3 Myr. Compared to EW([O III]), we find a moderate correlation ($\rho = 0.46$, $p \sim 0$) such that galaxies with high EWs tend to show high SFR$_{3\,\rm Myr}$/SFR$_{100\,\rm Myr}$. Additionally, galaxies with high burstiness tend to show high SFR$_{3\,\rm Myr}$ ($\rho = 0.42$, $p = 2.6 \times 10^{-9}$). This suggests that EW is regulated not only by the burstiness of the system but also by the most recent SFR. An enhancement in the burstiness of a system in galaxies with elevated EW(Hα) has been found in samples of Hα emitters at $z \sim 2$ and $z \sim 4{-}6$ (Navarro-Carrera et al. 2026), and in low-mass galaxies $0.7 < z < 1.5$ (Atek et al. 2022). The high burstiness observed in a subsample of EELGs with broad [O III] emission and high EWs is consistent with a scenario in which these systems generate the feedback necessary to facilitate the escape of LyC radiation.

7.5. The primary drivers of extreme EWs

To isolate the intrinsic correlation between EW([O III]) and each parameter explored in Sects. 7.1, 7.3 and 7.4, we performed a partial Spearman correlation analysis by regressing each variable against the others and correlating the resulting residuals. This eliminates the influence of the other parameters, enabling us to evaluate the direct correlations between each variable and EW([O III]). To this analysis, we use the *statsmodels* package. We find that EW([O III]) shows a moderate positive correlation with both sSFR ($\rho = 0.42$, $p = 1.3 \times 10^{-4}$) and $\Sigma_{\rm SFR}$ ($\rho = 0.41$, $p = 2.2 \times 10^{-4}$) even after controlling for the other parameters, indicating that the EW([O III]) is primarily driven by star formation activity. In contrast, no significant correlation is found with effective radius ($\rho = -0.09$, $p = 0.43$) or burstiness ($\rho \sim 0$, $p = 0.93$), suggesting that structural parameters and specific degree of burstiness have little direct impact on EW([O III]) in this sample. However, we note that our sample is biased toward extreme EWs, and the strength of the correlations may change when including galaxies with lower EWs. A summary of the resulting partial corrrelations are reported in Table 2.

Overall, EELGs exhibit elevated sSFRs and $\Sigma_{\rm SFR}$. These properties suggest that intense star formation activity occurring within small spatial scales may be a key factor driving their extreme EWs. Additionally, high levels of burstiness, indicated by elevated $\rm SFR_{3\,Myr}/SFR_{100\,Myr}$ ratios, might further enhance the EWs, although our partial correlation analysis shows that sSFR and $\Sigma_{\rm SFR}$ are the primary drivers, while burstiness has no significant independent effect.

8. Summary and conclusions

We analysed a sample of 160 EELGs at $z \sim 4-9$, including 127 observed with NIRSpec/PRISM and 81 with NIRSpec/G395M, drawn from the CAPERS, CEERS, and RUBIES surveys. These galaxies were initially identified as EELG candidates from NIRCam photometry (Llerena et al. 2024). Our results can be summarized as follows:

1. We found a high success rate of 89% for the selection criteria proposed in Llerena et al. (2024) to identify EELGs at $z \sim 4-9$ with EW([O III]+Hβ) > 680 Å. In the confirmed extreme EELGs, the median EW([OIII]+Hβ) = 1616 Å and the median EW(Hα)=763 Å. Photometric redshifts are confirmed with a mean difference $z_{\rm phot} - z_{\rm spec} = 0.13$.
2. EELGs show a median $\log(M_\star/M_\odot) = 8.26$ and are scattered above the main sequence of SF galaxies at $z \sim 6$ based on the Balmer-derived SFRs. They show a wide range of $\rm E(B-V) \sim 0 - 0.46$ with no correlation with EW([O III]). They also show a wide range of β slopes with a median $\beta = -2.0$. Only 7% of EELGs have very blue slopes ($\beta < -2.6$), which are bluer than the limit expected from star formation and nebular continuum emission. However, this fraction is not statistically significant at the 1σ level.
3. Emission-line diagnostics (OHNO, MEx diagrams) suggest that massive stars are the dominant ionizing source in EELGs. An AGN contribution cannot be fully excluded in 14% of the sample, and evidence for BLAGNs is found in a small fraction (4%) of the sample.
4. EELGs are efficient producers of ionizing photons with a median $\log(\xi_{\rm ion}\ [\rm Hz\ erg^{-1}]) = 25.37$, which is slightly higher than the mean value found for SF galaxies at similar redshift. However, the escape of LyC photons, indirectly inferred from Cox models, is not particularly efficient. Only 16% of EELGs show high escape fractions >5% of both Lyα and LyC photons, while half (49%) are likely not strong LyC leakers ($\rm fesc_{LyC} < 5\%$). This is supported by the lack of Lyα emission in 82% of the sample and the fact that the median inferred $\rm fesc_{LyC}$=5% is not particularly elevated. However, the escape of LyC photons is enhanced in EELGs with sSFR>25Gyr^{-1} and $r_{\rm opt} < 200$ pc with a median $\rm fesc_{LyC}$=11.8%.
5. These results imply that EELGs play a non-negligible role in the total ionizing emissivity required to sustain hydrogen reionization, with a median contribution of approximately 16 – 40%. We emphasize, however, that this estimate relies on extrapolations into the very-faint UV regime, where the median properties of SF galaxies and EELGs remain highly uncertain.
6. EELGs exhibit very high sSFRs, with a median value of 43 Gyr^{-1}, along with very high $\Sigma_{\rm SFR}$, with a median value of 10.7 $M_\odot$ yr^{-1} kpc^{-2} and compact $r_{\rm opt}$, with a median of 0.49 kpc. These properties suggest that intense star formation activity occurring within small spatial scales may be a key factor driving their extreme EWs. Additionally, high burstiness, traced by the ratio $\rm SFR_{3\mathit{Myr}}/SFR_{100\mathit{Myr}}$, might enhance the observed EWs. However, sSFR and $\Sigma_{\rm SFR}$ are likely to be the primary drivers.

Overall, EELGs are low-mass systems characterized by elevated and compact star formation with a recent burst. They are efficient producers of ionizing photons; however, while a subset of the population exhibits high escape fractions of Lyα and LyC photons, they are not uniformly strong leakers with $\rm fesc_{LyC} > 5\%$. This may be attributed to the presence of dust within the ISM, as suggested by the relatively moderate (i.e. not extremely blue) UV continuum slopes observed in the sample since β seems to be an important indicator of $\rm fesc_{LyC}$ (Chisholm et al. 2022; Giovinazzo et al. 2026). Notably, in compact super-Eddington galaxies, the escape of LyC photons is enhanced.

Data availability

Table A.1 is available at the CDS via `https://cdsarc.cds.unistra.fr/viz-bin/cat/J/A+A/708/A152`

Acknowledgements. We thank the anonymous referee for the thorough review and constructive suggestions that significantly improved this paper. We also thank Sophia Flury for valuable feedback and insightful comments, which helped refine our interpretation of the results. MLl acknowledges support from the INAF Large Grant 2022 "Extragalactic Surveys with JWST" (PI L. Pentericci), the PRIN 2022 MUR project 2022CB3PJ3 – First Light And Galaxy aSsembly (FLAGS) funded by the European Union – Next Generation EU, the INAF Mini-grant 2024 "Galaxies in the epoch of Reionization and their analogs at lower redshift" (PI M. Llerena), and the Large Grant RF 2023 F.O. 1.05.23.01.11 "The MOONS Extragalactic Survey". RA acknowledges support of Grant PID2023-147386NB-I00 funded by MICIU/AEI/10.13039/501100011033 and by ERDF/EU, and the Severo Ochoa award to the IAA-CSIC CEX2021-001131-S. This work is based on observations made with the NASA/ESA/CSA *James Webb* Space Telescope, obtained at the Space Telescope Science Institute, which is operated by the Association of Universities for Research in Astronomy, Incorporated, under NASA contract NAS5-03127. Support for program number GO-6368 was provided through a grant from the STScI under NASA contract NAS5-03127. The data were obtained from the Mikulski Archive for Space Telescopes (MAST) at the Space Telescope Science Institute. These observations are associated with program #6368, and can be accessed via doi. Some of the data products presented herein were retrieved from the Dawn JWST Archive (DJA). DJA is an initiative of the Cosmic Dawn Center (DAWN), which is funded by the Danish National Research Foundation under grant DNRF140. These observations are associated with programs #1345, #2750, and #4233. This work has made extensive use of Python packages astropy (Astropy Collaboration 2018), numpy (Harris et al. 2020), Matplotlib (Hunter 2007) and LiMe (Fernández et al. 2024).

References

Amorín, R. O., Pérez-Montero, E., & Vílchez, J. M. 2010, ApJ, 715, L128
Amorín, R., Pérez-Montero, E., Contini, T., et al. 2015, A&A, 578, A105
Amorín, R. O., Rodríguez-Henríquez, M., Fernández, V., et al. 2024, A&A, 682, L25
Arevalo-Gonzalez, F., Braun, T., Trussler, J., et al. 2025, MNRAS, 544, 2737
Asada, Y., Fujimoto, S., Chisholm, J., et al. 2026, ApJ, submitted [arXiv:`2601.20045`]
Asplund, M., Grevesse, N., Sauval, A. J., & Scott, P. 2009, ARA&A, 47, 481
Astropy Collaboration (Price-Whelan, A. M., et al.) 2018, AJ, 156, 123
Atek, H., Furtak, L. J., Oesch, P., et al. 2022, MNRAS, 511, 4464
Atek, H., Labbé, I., Furtak, L. J., et al. 2024, Nature, 626, 975

Backhaus, B. E., Trump, J. R., Cleri, N. J., et al. 2022, ApJ, 926, 161
Baldwin, J. A., Phillips, M. M., & Terlevich, R. 1981, PASP, 93, 5
Begley, R., Cullen, F., McLure, R. J., et al. 2024, MNRAS, 527, 4040
Begley, R., McLure, R. J., Cullen, F., et al. 2026, MNRAS, 545, staf1995
Begley, R., McLure, R. J., Cullen, F., et al. 2025, MNRAS, 537, 3245
Bertin, E., & Arnouts, S. 1996, A&AS, 117, 393
Bian, F., Kewley, L. J., & Dopita, M. A. 2018, ApJ, 859, 175
Bouwens, R. J., Oesch, P. A., Stefanon, M., et al. 2021, AJ, 162, 47
Boyett, K., Bunker, A. J., Curtis-Lake, E., et al. 2024, MNRAS, 535, 1796
Brooks, M., Simons, R. C., Trump, J. R., et al. 2025, ApJ, 986, 177
Bruzual, G., & Charlot, S. 2003, MNRAS, 344, 1000
Bunker, A. J., Saxena, A., Cameron, A. J., et al. 2023, A&A, 677, A88
Calabrò, A., Amorín, R., Fontana, A., et al. 2017, A&A, 601, A95
Calabrò, A., Pentericci, L., Feltre, A., et al. 2023, A&A, 679, A80
Calabrò, A., Castellano, M., Zavala, J. A., et al. 2024a, ApJ, 975, 245
Calabrò, A., Pentericci, L., Santini, P., et al. 2024b, A&A, 690, A290
Calzetti, D., Kinney, A. L., & Storchi-Bergmann, T. 1994, ApJ, 429, 582
Calzetti, D., Armus, L., Bohlin, R. C., et al. 2000, ApJ, 533, 682
Cardamone, C., Schawinski, K., Sarzi, M., et al. 2009, MNRAS, 399, 1191
Carnall, A. C., McLure, R. J., Dunlop, J. S., & Davé, R. 2018, MNRAS, 480, 4379
Carniani, S., Venturi, G., Parlanti, E., et al. 2024, A&A, 685, A99
Carr, C. A., Cen, R., Scarlata, C., et al. 2025, ApJ, 982, 137
Chabrier, G. 2003, PASP, 115, 763
Chen, Z., Stark, D. P., Mason, C. A., et al. 2025, ApJ, submitted [arXiv:2505.24080]
Chevallard, J., Charlot, S., Senchyna, P., et al. 2018, MNRAS, 479, 3264
Chisholm, J., Saldana-Lopez, A., Flury, S., et al. 2022, MNRAS, 517, 5104
Cleri, N. J., Yang, G., Papovich, C., et al. 2023, ApJ, 948, 112
Cleri, N. J., Olivier, G. M., Backhaus, B. E., et al. 2025, ApJ, 994, 146
Coil, A. L., Aird, J., Reddy, N., et al. 2015, ApJ, 801, 35
Cole, J. W., Papovich, C., Finkelstein, S. L., et al. 2025, ApJ, 979, 193
Cooper, R. A., Caputi, K. I., Iani, E., et al. 2025, ApJ, 994, 102
Cullen, F., McLeod, D. J., McLure, R. J., et al. 2024, MNRAS, 531, 997
Daikuhara, K., Morishita, T., Kodama, T., et al. 2025, ApJ, 989, 71
Davis, M., Guhathakurta, P., Konidaris, N. P., et al. 2007, ApJ, 660, L1
Davis, K., Trump, J. R., Simons, R. C., et al. 2024, ApJ, 974, 42
De Barros, S., Oesch, P. A., Labbé, I., et al. 2019, MNRAS, 489, 2355
de Graaff, A., Brammer, G., Weibel, A., et al. 2025, A&A, 697, A189
Dottorini, D., Calabrò, A., Pentericci, L., et al. 2025, A&A, 698, A234
Du, X., Shapley, A. E., Tang, M., et al. 2020, ApJ, 890, 65
Eldridge, J. J., & Stanway, E. R. 2022, ARA&A, 60, 455
Endsley, R., Stark, D. P., Bouwens, R. J., et al. 2022, MNRAS, 517, 5642
Endsley, R., Stark, D. P., Whitler, L., et al. 2023, MNRAS, 524, 2312
Endsley, R., Stark, D. P., Whitler, L., et al. 2024, MNRAS, 533, 1111
Fabozzi, F. J., Focardi, S. M., Rachev, S. T.& Arshanapalli, B. G. 2014, The Basics of Financial Econometrics: Tools, Concepts, and Asset Management Applications (Wiley)
Fan, X., Strauss, M. A., Becker, R. H., et al. 2006, AJ, 132, 117
Fernández, V., Amorín, R., Firpo, V., & Morisset, C. 2024, A&A, 688, A69
Ferrara, A. 2024, A&A, 684, A207
Ferrara, A., Giavalisco, M., Pentericci, L., et al. 2025, Open J. Astrophys., 8, 125
Feuillet, L. M., Meléndez, M., Kraemer, S., et al. 2024, ApJ, 962, 104
Finkelstein, S. L., D'Aloisio, A., Paardekooper, J.-P., et al. 2019, ApJ, 879, 36
Finkelstein, S. L., Bagley, M. B., Ferguson, H. C., et al. 2023, ApJ, 946, L13
Finkelstein, S. L., Leung, G. C. K., Bagley, M. B., et al. 2024, ApJ, 969, L2
Finkelstein, S. L., Bagley, M. B., Arrabal Haro, P., et al. 2025, ApJ, 983, L4
Flury, S. R., Jaskot, A. E., Ferguson, H. C., et al. 2022a, ApJS, 260, 1
Flury, S. R., Jaskot, A. E., Ferguson, H. C., et al. 2022b, ApJ, 930, 126
Flury, S. R., Arellano-Córdova, K. Z., Moran, E. C., & Einsig, A. 2025a, MNRAS, 543, 3367
Flury, S. R., Jaskot, A. E., Saldana-Lopez, A., et al. 2025b, ApJ, 985, 128
Foreman-Mackey, D., Hogg, D. W., Lang, D., & Goodman, J. 2013, PASP, 125, 306
Gardner, J. P., Mather, J. C., Clampin, M., et al. 2006, Space Sci. Rev., 123, 485
Gardner, J. P., Mather, J. C., Abbott, R., et al. 2023, PASP, 135, 068001
Giovinazzo, E., Oesch, P. A., Weibel, A., et al. 2026, A&A, 707, A352
Grogin, N. A., Kocevski, D. D., Faber, S. M., et al. 2011, ApJS, 197, 35
Harikane, Y., Zhang, Y., Nakajima, K., et al. 2023, ApJ, 959, 39
Harris, C. R., Millman, K. J., van der Walt, S. J., et al. 2020, Nature, 585, 357
Hayes, M. 2015, PASA, 32, e027
Heintz, K. E., Watson, D., Brammer, G., et al. 2024, Science, 384, 890
Hogarth, L., Amorín, R., Vílchez, J. M., et al. 2020, MNRAS, 494, 3541
Hunter, J. D. 2007, Comput. Sci. Eng., 9, 90
Hviding, R. E., de Graaff, A., Miller, T. B., et al. 2025, A&A, 702, A57
Iyer, K., Gawiser, E., Davé, R., et al. 2018, ApJ, 866, 120
Izotov, Y. I., Guseva, N. G., & Thuan, T. X. 2011, ApJ, 728, 161
Izotov, Y. I., Guseva, N. G., Fricke, K. J., & Henkel, C. 2016, MNRAS, 462, 4427
Izotov, Y. I., Schaerer, D., Worseck, G., et al. 2020, MNRAS, 491, 468
Izotov, Y. I., Worseck, G., Schaerer, D., et al. 2021, MNRAS, 503, 1734
Jakobsen, P., Ferruit, P., Alves de Oliveira, C., et al. 2022, A&A, 661, A80
Jaskot, A. E. 2025, ARA&A, 63, 45
Jaskot, A. E., Silveyra, A. C., Plantinga, A., et al. 2024a, ApJ, 972, 92
Jaskot, A. E., Silveyra, A. C., Plantinga, A., et al. 2024b, ApJ, 973, 111
Juneau, S., Dickinson, M., Alexander, D. M., & Salim, S. 2011, ApJ, 736, 104
Juneau, S., Bournaud, F., Charlot, S., et al. 2014, ApJ, 788, 88
Kennicutt, R. C., & Evans, N. J. 2012, ARA&A, 50, 531
Kewley, L. J., & Dopita, M. A. 2002, ApJS, 142, 35
Kocevski, D. D., Finkelstein, S. L., Barro, G., et al. 2025, ApJ, 986, 126
Koekemoer, A. M., Faber, S. M., Ferguson, H. C., et al. 2011, ApJS, 197, 36
Kokorev, V., Chávez Ortiz, Ó. A., Taylor, A. J., et al. 2025, ApJ, 988, L10
Komarova, L., Oey, M. S., Marques-Chaves, R., et al. 2025, ApJ, 994, 192
Koyama, Y., Shimakawa, R., Yamamura, I., Kodama, T., & Hayashi, M. 2019, PASJ, 71, 8
Kroupa, P. 2001, MNRAS, 322, 231
Laseter, I. H., Maseda, M. V., Simmonds, C., et al. 2025, ApJ, 988, 73
Lecroq, M., Charlot, S., Bressan, A., et al. 2025, A&A, 695, A17
Leitherer, C., & Heckman, T. M. 1995, ApJS, 96, 9
Leja, J., Carnall, A. C., Johnson, B. D., Conroy, C., & Speagle, J. S. 2019, ApJ, 876, 3
León Contreras, A., Amorín, R., Llerena, M., & Fernández, V. 2026, A&A, 707, A13
Llerena, M., Amorín, R., Cullen, F., et al. 2022, A&A, 659, A16
Llerena, M., Amorín, R., Pentericci, L., et al. 2023, A&A, 676, A53
Llerena, M., Amorín, R., Pentericci, L., et al. 2024, A&A, 691, A59
Llerena, M., Pentericci, L., Napolitano, L., et al. 2025, A&A, 698, A302
Madau, P., & Dickinson, M. 2014, ARA&A, 52, 415
Madau, P., Haardt, F., & Rees, M. J. 1999, ApJ, 514, 648
Marchi, F., Pentericci, L., Guaita, L., et al. 2017, A&A, 601, A73
Mascia, S., Pentericci, L., Calabrò, A., et al. 2024, A&A, 685, A3
Mascia, S., Pentericci, L., Llerena, M., et al. 2025, A&A, 701, A122
Maseda, M. V., van der Wel, A., Rix, H.-W., et al. 2018, ApJ, 854, 29
Maseda, M. V., Bacon, R., Lam, D., et al. 2020, MNRAS, 493, 5120
Mason, C. A., & Gronke, M. 2020, MNRAS, 499, 1395
Matthee, J., Mackenzie, R., Simcoe, R. A., et al. 2023, ApJ, 950, 67
McGrath, E. J., Finkelstein, S. L., Barro, G., et al. 2026, ApJ, 999, L6
Morales, A. M., Finkelstein, S. L., Arrabal Haro, P., et al. 2025, ApJ, 994, 212
Nandra, K., Laird, E. S., Aird, J. A., et al. 2015, ApJS, 220, 10
Napolitano, L., Castellano, M., Pentericci, L., et al. 2025, A&A, 693, A50
Napolitano, L., Pentericci, L., Dickinson, M., et al. 2026, A&A, 708, A102
Napolitano, L., Pentericci, L., Santini, P., et al. 2024, A&A, 688, A106
Navarro-Carrera, R., Rinaldi, P., Caputi, K. I., et al. 2026, ApJ, 996, 70
Ning, Y., Cai, Z., Jiang, L., et al. 2023, ApJ, 944, L1
Ning, Y., Cai, Z., Lin, X., et al. 2024, ApJ, 963, L38
Oke, J. B., & Gunn, J. E. 1983, ApJ, 266, 713
Pahl, A. J., Shapley, A., Reddy, N. A., et al. 2026, ApJ, 996, 37
Papovich, C., Cole, J. W., Yang, G., et al. 2023, ApJ, 949, L18
Peng, C. Y., Ho, L. C., Impey, C. D., & Rix, H.-W. 2002, AJ, 124, 266
Peng, C. Y., Ho, L. C., Impey, C. D., & Rix, H.-W. 2010, AJ, 139, 2097
Pérez-Montero, E. 2017, PASP, 129, 043001
Pérez-Montero, E., Amorín, R., Sánchez Almeida, J., et al. 2021, MNRAS, 504, 1237
Raiter, A., Schaerer, D., & Fosbury, R. A. E. 2010, A&A, 523, A64
Rieke, M. J., Kelly, D. M., Misselt, K., et al. 2023, PASP, 135, 028001
Roberts-Borsani, G., Treu, T., Shapley, A., et al. 2024, ApJ, 976, 193
Robertson, B. E. 2022, ARA&A, 60, 121
Saldana-Lopez, A., Schaerer, D., Chisholm, J., et al. 2022, A&A, 663, A59
Saldana-Lopez, A., Chisholm, J., Gazagnes, S., et al. 2025, MNRAS, 544, 132
Sánchez Almeida, J., Terlevich, R., Terlevich, E., Cid Fernandes, R., & Morales-Luis, A. B. 2012, ApJ, 756, 163
Sanders, R. L., Shapley, A. E., Topping, M. W., Reddy, N. A., & Brammer, G. B. 2024, ApJ, 962, 24
Shapley, A. E., Sanders, R. L., Reddy, N. A., Topping, M. W., & Brammer, G. B. 2023, ApJ, 954, 157
Smit, R., Bouwens, R. J., Franx, M., et al. 2015, ApJ, 801, 122
Speagle, J. S., Steinhardt, C. L., Capak, P. L., & Silverman, J. D. 2014, ApJS, 214, 15
Stanton, T. M., Cullen, F., McLure, R. J., et al. 2024, MNRAS, 532, 3102
Tang, M., Stark, D. P., Chevallard, J., & Charlot, S. 2019, MNRAS, 489, 2572
Tang, M., Stark, D. P., & Ellis, R. S. 2022, MNRAS, 513, 5211
Tang, M., Stark, D. P., Chen, Z., et al. 2023, MNRAS, 526, 1657
Tang, M., Stark, D. P., Ellis, R. S., et al. 2024, ApJ, 972, 56
Taylor, A. J., Finkelstein, S. L., Kocevski, D. D., et al. 2025a, ApJ, 986, 165

Taylor, A. J., Kokorev, V., Kocevski, D. D., et al. 2025b, ApJ, 989, L7
van der Wel, A., Straughn, A. N., Rix, H. W., et al. 2011, ApJ, 742, 111
Vanzella, E., De Barros, S., Cupani, G., et al. 2016, ApJ, 821, L27
Vanzella, E., Loiacono, F., Bergamini, P., et al. 2023, A&A, 678, A173
Vanzella, E., Loiacono, F., Messa, M., et al. 2024, A&A, 691, A251
Verhamme, A., Orlitová, I., Schaerer, D., & Hayes, M. 2015, A&A, 578, A7
Witstok, J., Jakobsen, P., Maiolino, R., et al. 2025, Nature, 639, 897
Wright, G. S., Wright, D., Goodson, G. B., et al. 2015, PASP, 127, 595
Xu, X., Henry, A., Heckman, T., et al. 2023, ApJ, 943, 94
Yang, G., Papovich, C., Bagley, M. B., et al. 2023, ApJ, 956, L12
Yung, L. Y. A., Somerville, R. S., Finkelstein, S. L., Popping, G., & Davé, R. 2019, MNRAS, 483, 2983
Yung, L. Y. A., Somerville, R. S., Finkelstein, S. L., et al. 2020a, MNRAS, 496, 4574
Yung, L. Y. A., Somerville, R. S., Popping, G., & Finkelstein, S. L. 2020b, MNRAS, 494, 1002
Zamora, S., Carniani, S., Bertola, E., et al. 2025, A&A, submitted [arXiv:2512.09022]
Zhu, P., Kewley, L. J., & Sutherland, R. S. 2023, ApJ, 954, 175

---

[1] INAF – Osservatorio Astronomico di Roma, Via di Frascati 33, 00078 Monte Porzio Catone, Italy
[2] Instituto de Astrofísica de Andalucía (CSIC), Apartado 3004, 18080 Granada, Spain
[3] Scuola Normale Superiore, Piazza dei Cavalieri 7, 50126 Pisa, Italy
[4] NSF NOIRLab, 950 N. Cherry Ave., Tucson, AZ 85719, USA
[5] Dipartimento di Fisica, Università di Roma Sapienza, Città Universitaria di Roma – Sapienza, Piazzale Aldo Moro, 2, 00185 Roma, Italy
[6] Institute of Science and Technology Austria (ISTA), Am Campus 1, A-3400 Klosterneuburg, Austria
[7] Astrophysics Science Division, NASA Goddard Space Flight Center, 8800 Greenbelt Rd, Greenbelt, MD 20771, USA
[8] Armagh Observatory and Planetarium, College Hill, Armagh, BT61 9DG N. Ireland, UK
[9] Department of Astronomy and Astrophysics, The Pennsylvania State University, University Park, PA 16802, USA
[10] Institute for Computational and Data Sciences, The Pennsylvania State University, University Park, PA 16802, USA
[11] Institute for Gravitation and the Cosmos, The Pennsylvania State University, University Park, PA 16802, USA
[12] Department of Physics, 196 Auditorium Road, Unit 3046, University of Connecticut, Storrs, CT 06269, USA
[13] Los Alamos National Laboratory, Los Alamos, NM 87545, USA
[14] Department of Physics and Astronomy, Texas A&M University, College Station, TX 77843-4242, USA
[15] George P. and Cynthia Woods Mitchell Institute for Fundamental Physics and Astronomy, Texas A&M University, College Station, TX 77843-4242, USA
[16] Laboratory for Multiwavelength Astrophysics, School of Physics and Astronomy, Rochester Institute of Technology, 84 Lomb Memorial Drive, Rochester, NY 14623, USA
[17] Space Telescope Science Institute, 3700 San Martin Drive, Baltimore, MD 21218, USA
[18] Department of Physics and Astronomy, Colby College, Waterville, ME 04901, USA
[19] Institute for Astronomy, University of Edinburgh, Royal Observatory, Edinburgh EH9 3HJ, UK
[20] Department of Astronomy, The University of Texas at Austin, Austin, TX, USA
[21] Cosmic Frontier Center, The University of Texas at Austin, Austin, TX, USA
[22] School of Astronomy and Space Science, University of Chinese Academy of Sciences (UCAS), Beijing 100049, China
[23] National Astronomical Observatories, Chinese Academy of Sciences, Beijing 100101, China
[24] Institute for Frontiers in Astronomy and Astrophysics, Beijing Normal University, Beijing 102206, China

Appendix A: Summary of properties in the sample

In Table A.1 we provide information about the galaxies in the sample. We report their identification ID from the CEERS photometric catalogue and their spectroscopic ID (Spec ID) in each survey. We report their coordinates, the corresponding spectroscopic survey and disperser, spectroscopic redshifts, rest-frame EWs of bright emission lines (Hβ, [O III], and Hα), E(B–V) from SED modelling, sSFRs, β slopes, $M_{\rm UV}$, rest-frame optical effective radius, and the inferred $\rm fesc_{LyC}$ from the Cox models. The NLAGN candidates based on the OHNO diagram shown in Sect. 5.1 are flagged with an N. The EELGs in the sample classified as BLAGNs in Sect. 5.2 are flagged with a B, while the ones with evidence of a broad [O III] component are flagged with an O.

Appendix B: Gaussian fitting of [O III]+Hβ lines

Due to the wavelength-dependent spectral resolution of NIRSpec/PRISM, the [O III]+Hβ lines may appear blended or partially blended depending on the redshift of the source. In contrast, the higher spectral resolution of NIRSpec/MR (R$\sim$1000) allows the three lines to be well separated. Figure B.1 shows two examples of the Gaussian modelling of [O III]+Hβ lines using LiMe described in Sect. 2.2 for galaxies observed with NIRSpec/PRISM.

In the top panel, the [O III]+Hβ lines of galaxy ID 9482 are blended. This galaxy is the lowest-redshift source ($z_{\rm spec}$ = 3.96) in the CAPERS subsample, and the [O III]+Hβ lines fall at observed wavelengths corresponding to R$\sim$70. In the bottom panel, the spectrum of galaxy ID 44441, the highest-redshift source ($z_{\rm spec}$ = 8.73), shows the unblended [O III]+Hβ lines at observed wavelengths corresponding to R$\sim$270. These two cases correspond to the more extreme cases in terms of spectral resolution for these lines.

As described in Sect. 2.2, [O III]+Hβ lines are modelled as blended Gaussians, meaning that each line is represented by an individual Gaussian fit simultaneously. For the [O III]+Hβ complex, we assume the theoretical [O III]λ5007/[O III]λ4959 flux ratio of 2.94 and adopt the same velocity width for all lines. As shown in Fig. B.1, this approach allows us to recover the individual line components even in the lowest-resolution case.

Appendix C: Median spectrum of EELGs

To show the typical spectral features of EELGs, we constructed a median stacked spectrum of all 127 galaxies in our sample with PRISM observations. The stacking was performed using a non-weighted approach. Each individual spectrum was first shifted to the rest-frame using its spectroscopic redshift and then interpolated onto a common wavelength grid between 1000 and 7000 Å and considering the median redshift of the sample, z = 5.2. The spectra were subsequently normalized to the median flux within the 2700-2800 Å range. At each wavelength, the final stacked flux density was computed as the median of the individual flux densities, applying a 3-σ clipping to exclude outliers.

The 1-σ uncertainty on the stacked spectrum was estimated via bootstrap resampling: for each wavelength, the median flux was recalculated for 1000 random resamplings of the individual spectra, and the standard deviation of these medians was taken as the error. The resulting stacked spectrum is presented in Fig. C.1, where we indicate the positions of prominent emission lines, many of which are analysed in detail in this paper. This approach allows us to highlight the typical spectral features of the EELG population.

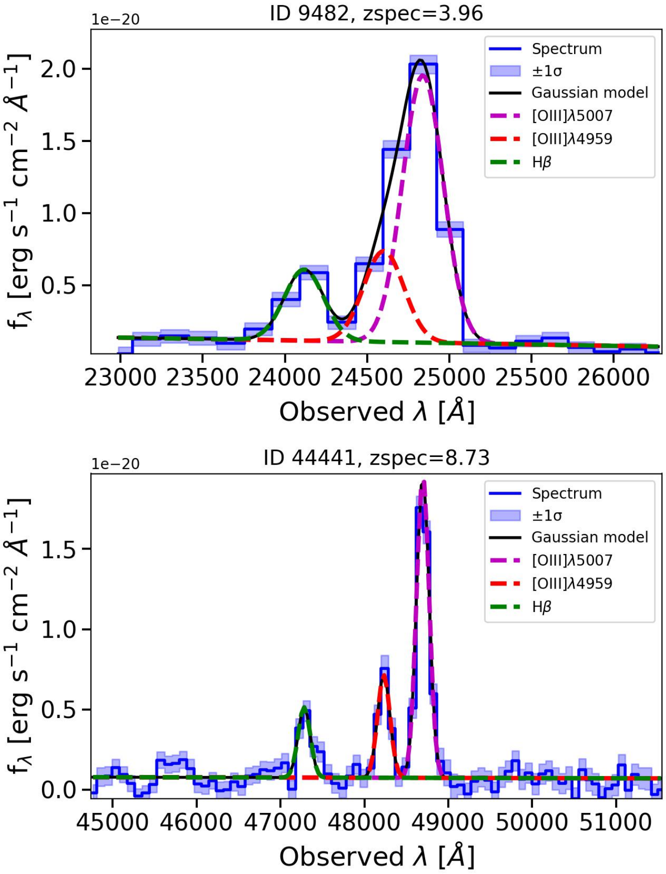

Fig. B.1. Showcases of Gaussian modelling of the [O III]+Hβ emission-line complex. *Top*: The lowest-redshift source in the CAPERS subsample, illustrating the case where the [O III]+Hβ lines are observed with a resolution R$\sim$ 70. *Bottom*: The highest-redshift source in the CAPERS subsample, representing the opposite extreme where the [O III]+Hβ emission is observed with a resolution R$\sim$ 270. In both panels, the observed NIRSpec/PRISM spectrum is shown as a blue solid line, with the shaded region indicating the 1σ uncertainty. The solid black curve represents the total best-fitting model to the [O III]+Hβ complex, while the magenta, red, and green dashed lines represent the individual Gaussian components of [O III]λ5007, [O III]λ4959, and Hβ, respectively.

We perform a similar approach with the 81 galaxies in the sample with MR spectra. In this case, we considered a common wavelength grid between 3600 and 7000 Å and considering the median redshift of the sample, z = 5.2. The individual spectra were normalized to the median flux within the 5100-6400 Å range. The resulting spectrum is shown in Fig. C.2.

Appendix D: Fluxes and EWs of emission lines

In Fig. D.1 we show the comparison between EW([O III]) and EW(Hβ). We find that galaxies exhibiting high EW([O III]) also tend to show correspondingly high EWs in the Balmer lines. This strong correlation (ρ = 0.78, $p \sim 0$) suggests a common source of ionization for both [O III] and the Balmer emission, most likely originating from intense star-forming activity. Our findings are consistent with recent results from the JADES survey, which examined EELGs over $3 < z < 9.5$ and reported similar EW behavior (Boyett et al. 2024). Furthermore, we note that a similar EW([O III])–EW(Hβ) relationship has been observed in

Table A.1. Properties of the sample, in order of decreasing EW([OIII]). The full table is available at the CDS.

ID	Flag[a]	Spec ID	RA deg	DEC deg	Survey*	$z_{\rm spec}$	EW(Hβ) Å	EW([O III]) Å	EW(Hα) Å	E(B-V)	log(sSFR) Gyr^{-1}	β	M_{UV}	$r_{\rm opt}$ kpc	log(fesc$_{\rm LyC}$)
59920	–	944720	214.88300	52.84042	R-M	7.823	501 ± 54	4131 ± 362	-	0.12	2.09 ± 0.15	-	-	0.19 ± 0.01	-
44733	–	956207	214.89393	52.87458	R-M	7.033	495 ± 171	3190 ± 509	-	0.06	1.99 ± 0.22	-	-	0.61 ± 0.06	-
59920	–	944720	214.88300	52.84042	R-P	7.829	248 ± 60	3150 ± 281	-	0.12	1.78 ± 0.18	$-2.12^{+0.10}_{-0.10}$	-20.55	0.19 ± 0.01	-0.26
59920	–	1027	214.88300	52.84042	C-P	7.829	295 ± 42	2834 ± 249	-	0.12	1.86 ± 0.15	-	-19.80	0.19 ± 0.01	-0.30

Notes. [a]Source classification flags: B=Classified as BLAGN; N=Possible AGN from OHNO diagram; O=EELG with evidence of broad [O III]. *Survey and disperser abbreviations: CA-P: CAPERS-PRISM, C-P: CEERS-PRISM, R-P: RUBIES-PRISM, C-M: CEERS-MR, R-M: RUBIES-MR.

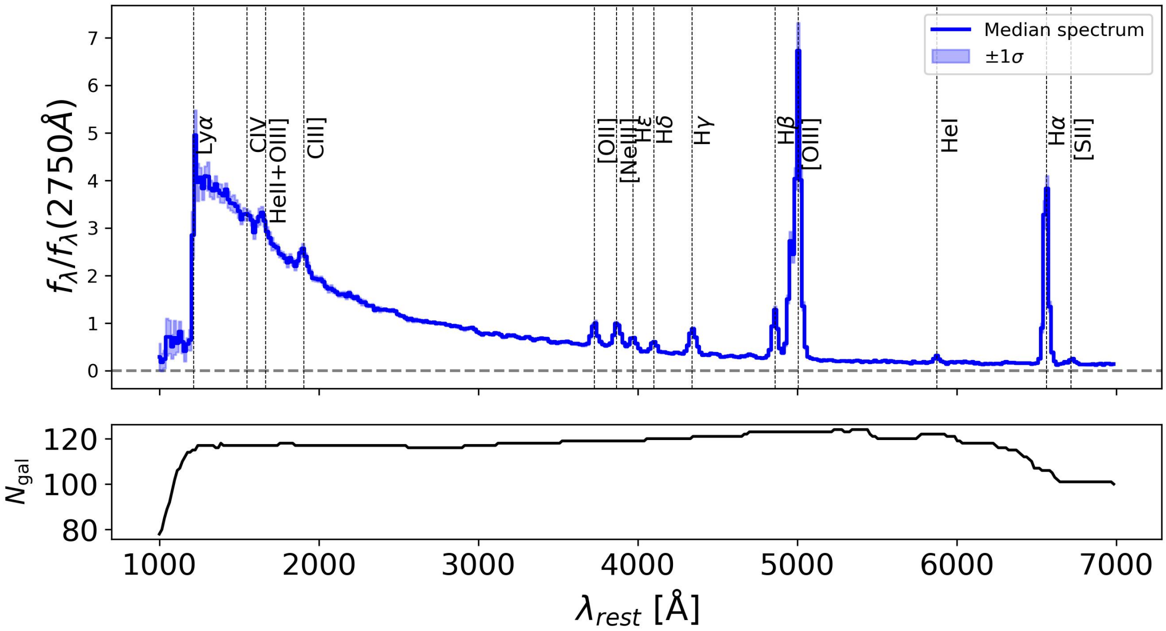

Fig. C.1. *Top*: Median spectrum of the EELGs in the sample with PRISM observations. The shaded region is the 1σ uncertainty. The vertical lines mark the position of typical emission lines. *Bottom*: Number of galaxies considered for the median spectrum.

LyC leakers at $z \sim 0.3$, where the emission line strengths are comparable to those in our EELG sample.

In Fig. D.2 we show a comparison between the observed fluxes (top panel) and EWs (bottom panel) in the subsample of galaxies that have PRISM and MR spectra. Regarding the observed fluxes, we find a very strong correlation ($\rho = 0.94$, $p \sim 0$) between the fluxes measured in the PRISM and the MR spectra for [O III], Hα and Hβ. We notice, however, that the fluxes measured in the PRISM spectra tend to be slightly higher than those measured in the MR spectra, with a median difference of 0.06 dex ($\sigma = 0.14$). Comparing the EWs of the same lines, we also find a very strong correlation ($\rho = 0.95$, $p \sim 0$) with a median difference of 0.06 dex ($\sigma = 0.17$) between the EWs measured from the PRISM and the MR spectra. This larger offset and scatter reflect the limitations in determining the faint continuum level in these galaxies.

Appendix E: SFRs from Balmer lines

In Fig. E.1 we show the comparison between the SFR obtained from SED fitting (average in the last 10 Myr) and from Balmer lines. We find a good agreement ($\rho = 0.85$, $p \sim 0$) between both parameters with a median log(SFR$_{\rm 10Myr}$)-log(SFR$_{\rm Balmer}$)=-0.16 dex ($\sigma = 0.24$ dex). This indicates that Balmer lines are tracers of the average SFR in the last 10Myr in our sample.

Appendix F: β from photometry versus spectra

In Fig. F.1 we show the difference in the UV β slopes using the methods described in Sect. 4.3 where we estimate β using the spectra or the photometry. These differences have been found in other works (e.g. Morales et al. 2025) when using only spectra or photometry to estimate the β slopes. We note that no wavelength-dependent correction was applied to the spectral flux calibration in this study. This choice is motivated by our finding that, on average, the correction factor remains consistent across all available filters, indicating that a single scaling provides a satisfactory match between photometric and spectroscopic measurements. Nevertheless, we cannot fully rule out a subtle wavelength dependence of the correction, which could contribute to some of the observed discrepancies between β estimated using spectra or photometry.

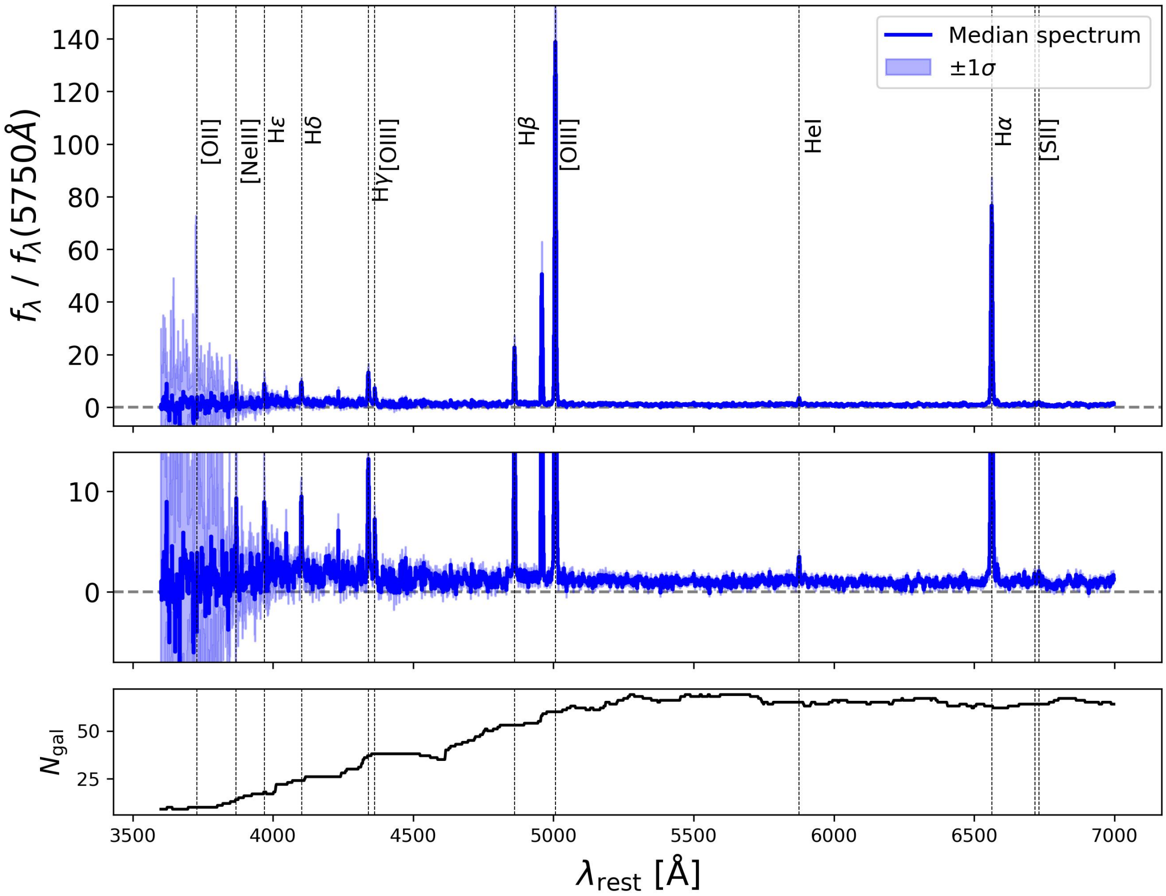

Fig. C.2. *Top*: Median spectrum of the EELGs in the sample with MR observations. The shaded region is the 1σ uncertainty. The vertical lines mark the position of typical emission lines. *Middle*: Zoomed-in view of the flux density for clarity. *Bottom*: Number of galaxies considered for the median spectrum.

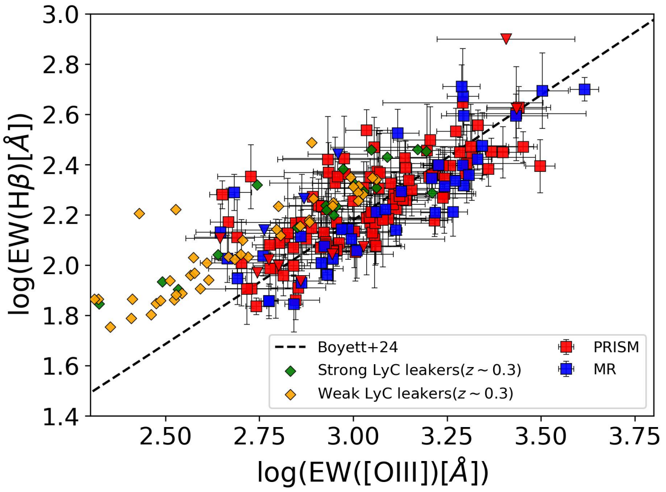

Fig. D.1. Comparison between EWs in the sample with PRISM (red squares) and MR (blue squares) spectra. The triangle symbols are upper limits due to low S/N of Hβ. The black dashed line is the relation from Boyett et al. (2024) for galaxies at $3 < z < 9.5$. Green and orange symbols are as in Fig. 3.

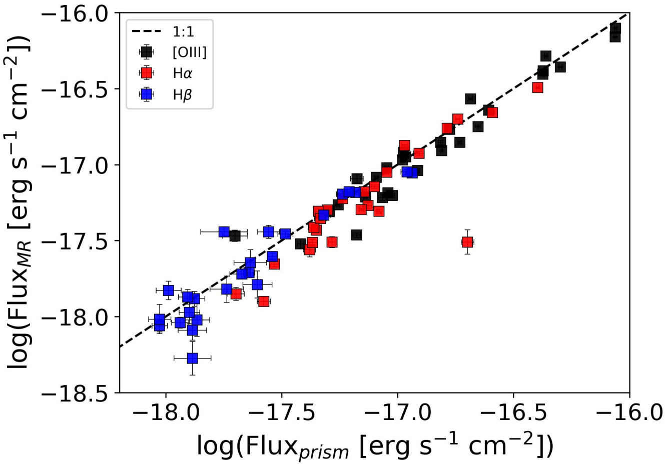

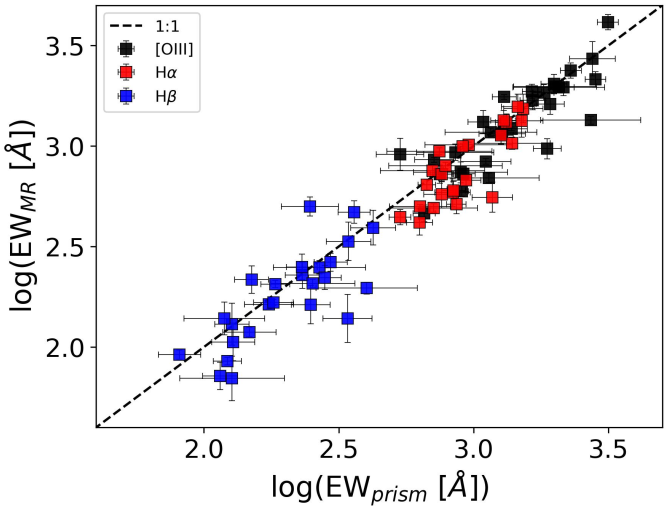

Fig. D.2. Comparison of fluxes (*top*) and EWs (*bottom*) of emission lines from PRISM and MR. In black, [O III], in red Hα, and in blue Hβ. The dashed black line is the 1:1 relation.

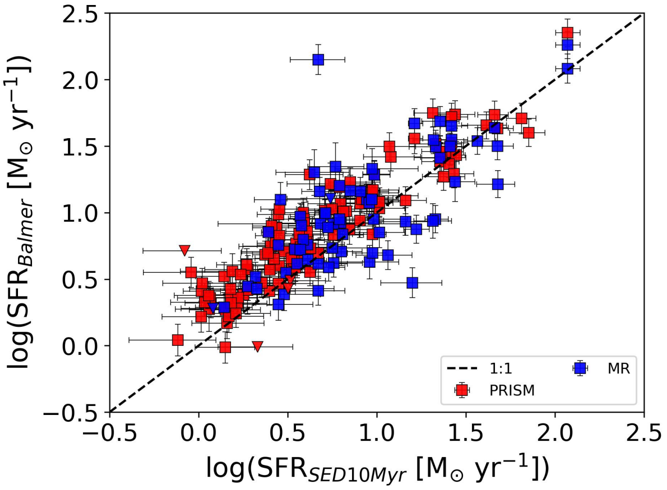

Fig. E.1. Comparison between SFRs from SED fitting (averaged over the last 10 Myr) and Balmer lines in the sample with PRISM (red squares) and MR (blue squares) spectra. Triangles indicate upper limits due to low Hβ S/N. The dashed black line shows the 1:1 relation.

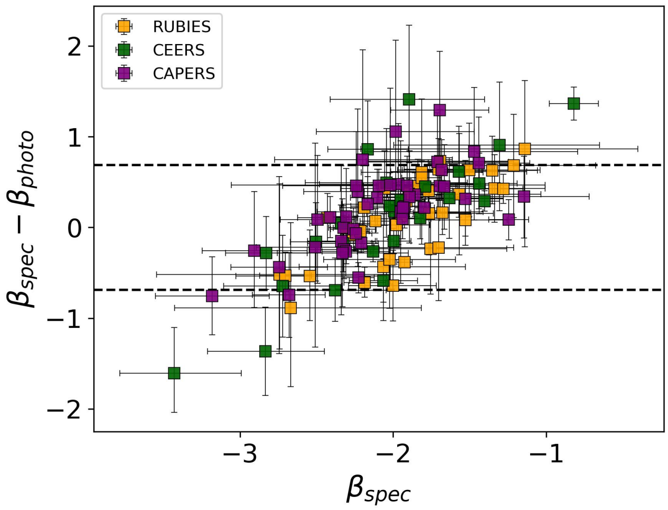

Fig. F.1. Difference in the UV β slopes estimated from spectra and photometry in the sample with PRISM spectra from the RUBIES (in orange), CEERS (in green) and CAPERS (in purple) surveys. The black dashed lines represent the median difference ± 1σ of the observed scatter.